2013

A Study of Inkjet Printed Line Morphology Using Volatile Ink with Non-zero Receding Contact Angle for Conductive Trace Fabrication

Chenchao Shou
Purdue University, gradcshou@gmail.com

Graduate School ETD Form 9
(Revised 12/07)

PURDUE UNIVERSITY
GRADUATE SCHOOL
Thesis/Dissertation Acceptance

This is to certify that the thesis/dissertation prepared

By Chenchao Shou

Entitled
A Study of Inkjet Printed Line Morphology Using Volatile Ink with Non-zero Receding Contact Angle for Conductive Trace Fabrication

For the degree of Master of Science in Mechanical Engineering

Is approved by the final examining committee:

George T. C. Chiu
Chair

Jeffrey Rhoads

Ronald G. Reifenberger

To the best of my knowledge and as understood by the student in the *Research Integrity and Copyright Disclaimer (Graduate School Form 20)*, this thesis/dissertation adheres to the provisions of Purdue University's "Policy on Integrity in Research" and the use of copyrighted material.

Approved by Major Professor(s): George T. C. Chiu

Approved by: David C. Anderson 04/24/2013
Head of the Graduate Program Date

A STUDY OF INKJET PRINTED LINE MORPHOLOGY USING VOLATILE INK WITH NON-ZERO RECEDING CONTACT ANGLE FOR CONDUCTIVE TRACE FABRICATION

A Thesis

Submitted to the Faculty

of

Purdue University

by

Chenchao Shou

In Partial Fulfillment of the

Requirements for the Degree

of

Master of Science in Mechanical Engineering

May 2013

Purdue University

West Lafayette, Indiana

ACKNOWLEDGMENTS

I would like to express my genuine gratitude to my advisor Professor George T. C. Chiu for his guidance on my Master's research. I would like to thank my committee members Professor Jeffrey Rhoads and Professor Ronald G. Reifenberger. I want to give my special thanks to my research collaborator William J. Boley for sharing his knowledge and experience. I also want to thank Patrick McCarthy for electrical resistance measurements, Professor James D. Litster and his graduate student Nathan B. Davis for providing the access to the tensiometer in their lab. Finally I thank Guoping Xiong and Stephen Hodson for assistance in microscope imaging and obtaining the ink and the substrate used in this research.

TABLE OF CONTENTS

LIST OF TABLES

LIST OF FIGURES

Figure Page

Figure Page

SYMBOLS

A_s	Surface Area
C	Molar Concentration of the Ink
d	Drop Position Offset Caused by Bidirectional Printing
d_p	Drop Pitch in a Print Pass
d_s	Dot Spacing in a Printed Line
D_0	Drop Diameter after Complete Evaporation
D_{eq}	Drop Diameter at the Equilibrium State
D_i	In-flight Droplet Diameter
D_m	Drop Maximum Spreading Diameter
D_n	Size of Ring Formation after the n^{th} Deposition
f_{max}	Highest Reliable Jetting Frequency
g	Gravitational Constant, 9.81 m/s^2
k	Constant in Tanner's Law
K	Drop Volume Proportionality Constant
L	Distance between Two Probes
m_d	Mass of Deposited Drops after Complete Evaporation
M	Molar Mass of the Solute
n_i^{TOTAL}	Total Moles of the i^{th} Component in the Surface System
n_i^{α}	Moles of the i^{th} Component in the α Phase
n_i^{β}	Moles of the i^{th} Component in the β Phase
n_p	Number of Passes in Multiple Pass Printing
N_d	Number of Deposited Droplets
N_p	Number of Pixels between Two Probes
R	Resistance
$R_{\square}$	Sheet Resistance

t_e	Single Drop Evaporation Time
t_w	Time Duration of Drop Wetting Phase
t_{w1}	Beginning Time of Drop Wetting Phase
t_{w2}	End Time of Drop Wetting Phase
T	Time for a Droplet to Reach the Substrate after Ejection
v_e	Droplet Ejection Speed
v_s	Scanning Speed
V_0	Volume of a Single Droplet
V_e	Equilibrium Bead Volume
V_{eq}	Drop Volume at the Equilibrium State
V_n	Bead Volume after the n^{th} Deposition
$\triangle V_{i,i+1}$	Bead Volumetric Loss from the i^{th} Deposition to the $(i+1)^{th}$ Deposition
$\triangle V_n$	1^{st} Order Forward Difference of Bead Volume
$\triangle^2 V_n$	2^{nd} Order Forward Difference of Bead Volume
W	Line Width
Z	Standoff Distance between the Print Head and the Substrate
γ_{LG}	Liquid-vapor Interfacial Energy
γ_{SG}	Solid-vapor Interfacial Energy
γ_{SL}	Solid-liquid Interfacial Energy
Γ_i	Surface Excess of Component i in a Liquid
μ	Viscosity of the Ink
μ_i	Chemical Potential of Component i in a Liquid
ρ	Density of the Ink
σ	Surface Tension of the Ink
τ	Time between Depositions of Adjacent Drops
θ_a	Advancing Contact Angle
θ_c	Drop Contact Angle
θ_e	Equilibrium Contact Angle

θ_r	Receding Contact Angle

ABBREVIATIONS

$ZRCA$	Zero Receding Contact Angle
$NRCA$	Non-zero Receding Contact Angle

ABSTRACT

Shou, Chenchao M.S.M.E, Purdue University, May 2013. A Study of Inkjet Printed Line Morphology Using Volatile Ink with Non-zero Receding Contact Angle for Conductive Trace Fabrication. Major Professor: George T. C. Chiu, School of Mechanical Engineering.

Inkjet printed lines on a homogeneous solid substrate are studied under the condition that ink evaporation is not negligible and the contact angle exhibits hysteresis with non-zero receding contact angle (NRCA). A new family of line instability is discovered, featured by formation of agglomerations within a line. The agglomeration is explained by a hydrodynamic flow that consistently drives a bead on the substrate towards fresh deposited droplets due to concentration-induced surface tension gradient. Morphologies of lines printed with multiple layers are also explored for the purpose of conductive trace fabrication. A non-uniform morphology is observed across a multi-layer line when the line is printed unidirectionally at a low jetting frequency. This non-uniformity is explained by considering the interaction between deposited droplets and bulk layer. An optimized multiple-pass printing is developed to produce a uniform line morphology while offering excellent printing efficiency and electrical conductivity.

1. INTRODUCTION

Inkjet printing is a widely used technology in the graphics industry to produce high-quality texts and colorful images thanks to its capability to deposit minute droplets in a precise and controlled way. In the recent decade, people have taken advantage of this capability to transform inkjet printing into a novel manufacturing tool for many functional devices in a wide range of fields, including printed electronics [1, 2], micro sensors and actuators [3, 4], solar cells and photovoltaics [5, 6], and biological cell patterning [7]. Compared to the conventional manufacturing processes, like photolithography and screen printing, inkjet printing has many advantages, such as dramatically reduced manufacturing cost, excellent flexibility and efficient use of materials [8–10].

Unlike the graphics application in which the printed patterns are discrete dots, successful application of inkjet printing to functional device fabrication typically requires one continuous solid deposit in the form of either a one-dimensional line or a two-dimensional film. A one-dimensional line is obviously the more basic geometry of the two and one direct application for the inkjet printed line is the fine electrically conductive trace. Therefore it's important to study the methodology of printing a smooth uniform continuous line.

To print such a line on a dry homogeneous solid surface is, however, not trivial, which requires fundamental understanding of how droplets interact with the solid surface and how printing parameters, like dot spacing and jetting frequency, influence the morphology of a printed line.

1.1 Contact Line, Contact Angle and Contact Angle Hysteresis

Contact line and contact angle are two basic terminologies to describe the interaction between a drop and a solid surface, as shown in Figure 1.1. On an ideal solid surface, the contact angle is uniquely determined by Young's Equation in the form of

$$\gamma_{SG} = \gamma_{SL} + \gamma_{LG} cos\theta_c, \tag{1.1}$$

where γ_{SG}, γ_{SL} and γ_{LG} are respectively the solid-vapor, solid-liquid and liquid-vapor interfacial energy. θ_c is the contact angle.

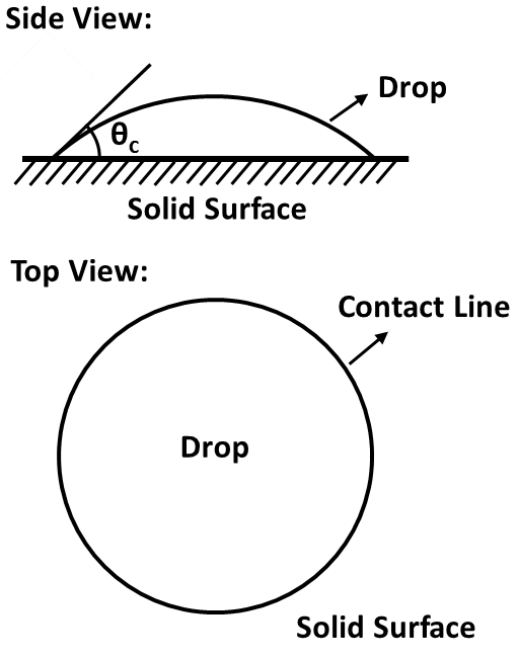

Figure 1.1. Illustration of contact angle and contact line. θ_c is the contact angle.

However, in practice the contact angle often times shows a wide range from the minimum contact angle known as the receding contact angle to the maximum contact angle known as the advancing contact angle. The advancing contact angle is defined as the contact angle above which the contact line advances whereas the receding contact angle, by definition, is the contact angle below which the contact line recedes. If the contact angle is in between the advancing and the receding contact angle, the

contact line is pinned (i.e. the contact line doesn't move). Contact angle hysteresis is the technical term referring to the non-uniqueness of the contact angle. This hysteresis is usually attributed to surface roughness, chemical heterogeneity and liquid adsorption [11–14]

1.2 Previous Printed Line Morphology Studies

Much work has been dedicated to elucidating the conditions that lead to different types of printed line morphologies. Early theoretical work by S. Davis [15] showed that a liquid bead on a solid surface was stable only if the contact line was arrested and the contact angle was smaller than $\frac{\pi}{2}$. Duineveld [16] studied the stability specifically for inkjet printed lines, where he discovered that a printed line always broke up into individual drops on a substrate with non-zero receding contact angle (NRCA) but could either be stable or have bulging instability with zero receding contact angle (ZRCA) depending on the relative transported flow rate through the ridge to the applied flow rate. Figure 1.2 illustrates these three types of line morphologies. Figure 1.3 shows the bulging instability for printed lines.

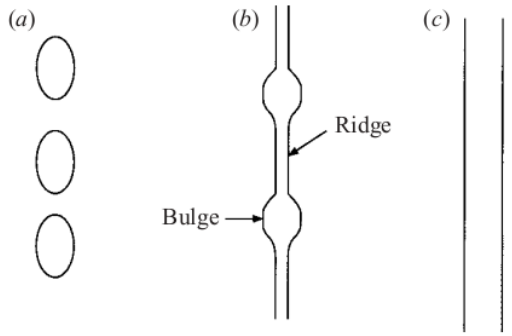

Figure 1.2. Illustration of three types of printed line morphologies by Duineveld [16]: (a) individual drops; (b) bulging instability; (c) stable.

It's worth noting that the experiments conducted by Duineveld used an aqueous solution, which had a relatively low vapor pressure and the proposed theoretical model

assumed that the evaporation of the ink was negligible during the course of printing. Stringer and Derby [17,18] extended the Duineveld's work by showing that the width of a stable line was always bounded by two limits. Soltman [19] studied the effect of substrate temperature on the printed line morphologies. All the experiments in the work of Stringer, Derby and Soltman were conducted under ZRCA conditions.

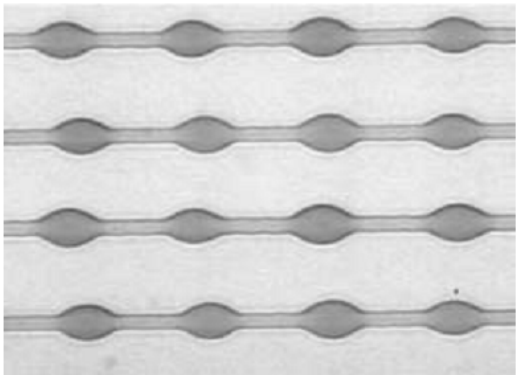

Figure 1.3. Bulging instability for printed lines by Duineveld [16].

1.3 Contributions of This Study

The previous line morphology studies [16–19] mainly focus on scenarios where ink evaporation is negligible or the receding contact angle is zero. The effect of ink evaporation on the line morphology, especially with NRCA condition, has not been well studied to the author's best knowledge.

In this work an experiment-based study of printed line morphologies will be presented using a volatile organometallic compound solution in the presence of contact angle hysteresis and NRCA. The impact of ink evaporation and NRCA on the line morphology will be elucidated. In addition to the morphologies of single-layer lines, the morphologies of lines printed with multiple layers will also be investigated, a topic that none of previous line morphology studies has ever explored. Of particular interest will be how the uniformity of multi-layer lines changes with different printing methods and the line uniformity will be then correlated with the electrical conduc-

tivity of the printed line. Finally an optimized printing routine will be developed for fine conductive trace fabrication to achieve excellent performances in both printing efficiency and electrical conductivity.

2. EXPERIMENTS

2.1 Inkjet Printing System

The inkjet printing system mainly consists of a high precision linear positioning stage (Anorad-WKY-C-150) with an encoder resolution of 0.5 μm, a Hewlett Packard Thermal Inkjet Picojet System (HP TIPS), a CCD camera (Sony XC-ST50), a SPiiPlus Series motion controller and a Z-axis translational stage (Edmund Optics R56-335) as shown in Figure 2.1.

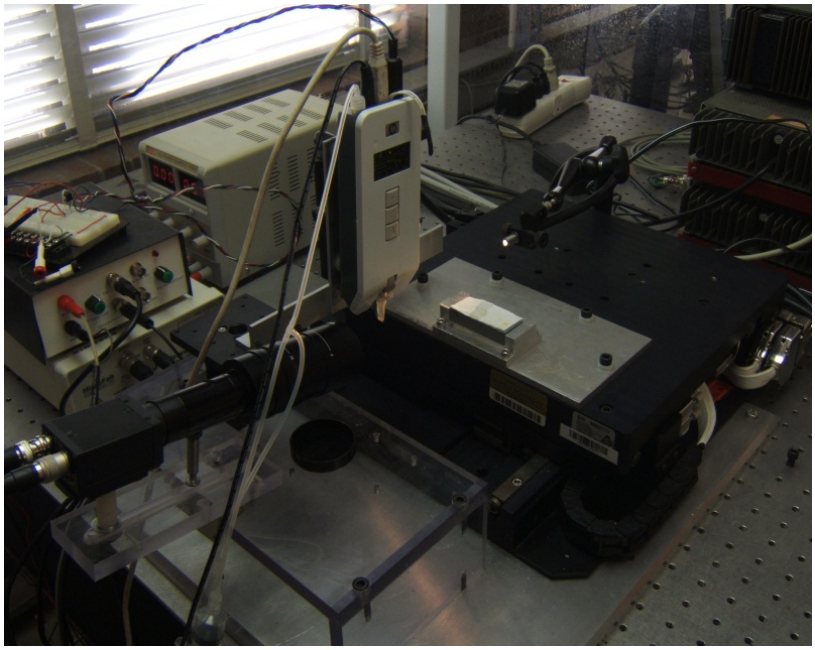

Figure 2.1. Photograph of the inkjet printing system used in this study.

The printing process is controlled through a graphical user interface (GUI) written in Visual C++ in the personal computer (PC). Prior to a printing job, in the GUI the user specifies the image to be printed, the printing start position in terms of the stage feedback position, the physical distance between adjacent pixels in the image

and the stage motion profile. Based on different printing requirements, the user can configure the TIPS controller accordingly through the GUI or the front panel of the controller. The GUI automatically translates the printing image information into a series of triggering positions and sends these triggering positions to the stage motion controller in a predefined controller language (ACSPL code). While printing a pattern, the print head is kept stationary and a substrate is moving along with the stage with a prescribed velocity profile. The motion controller sends a trigger to the TIPS controller whenever the stage reaches a prescribed triggering position. Upon receiving the trigger the TIPS controller sends one pulse to one nozzle or one pulse each to several nozzles depending on the preset configuration to eject one droplet or several droplets at the same time. In this manner the droplets are generated upon demand. A CCD camera interfaced with PC through National Instrument software provides the live video feedback of printing process. The back pressure of the liquid in the print head is regulated through a syringe pump system. The Z-axis stage is used to adjust the standoff distance between the print head and the substrate, which is typically kept fixed at about 250 μm. The connection between different components of inkjet printing system is illustrated in Figure 2.2.

2.2 Material Preparation and Measurements

The ink used in this study was palladium hexadecanethiolate ($Pd(SC_{16}H_{35})_2$) dissolved in toluene synthesized in-house. The ink was prepared by first mixing equal molars of Pd acetate and hexadecyl alkanethiol. The resulting mixture was then stirred vigorously. Following the reaction, the solution became viscous and the color was changed from yellow to orange yellow [20]. Finally the solution was diluted with pure toluene to the desired molar concentration.

The density of the ink was measured by first extracting a small amount of the ink with known volume from the ink container using a micropipette. The mass

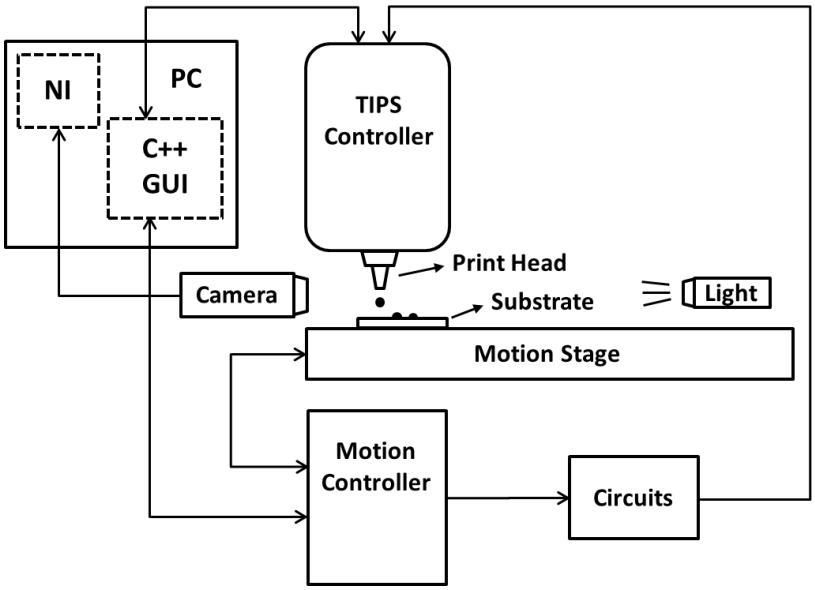

Figure 2.2. Illustration of connections between different components of the inkjet printing system.

corresponding to the extracted ink was measured by microbalance. The density was then obtained by dividing the measured mass by the known volume.

The surface tension of the ink was measured by the KRÜSS K100 tensiometer using the Wilhelmy plate method at the room temperature. The measurement was considered valid and accurate when the standard deviation of the last 10 measured data was smaller than 0.001 mN/m.

The viscosity of the ink was not measured but was estimated within a range using Mooney's equation [21].

The substrate was cut from a large silicon (Si) wafer with a thin silicon dioxide (SiO2) layer to a size of about 1 cm by 1 cm using a diamond tip. Prior to printing, they were cleaned in a sonication bath (Brandson 2510) with 5 min fresh acetone followed by 5 min fresh isopropanol and then blown dry by compressed air.

The advancing and the receding contact angle for the ink on the SiO2/Si substrate were measured by conducting sessile drop experiments. A droplet was first deposited onto the substrate by a syringe, which was held vertically with the tip of the needle located slightly above the surface of the substrate. By slowly pushing or pulling the syringe, the size of the drop on the substrate gradually increased or decreased. Multiple drop images were taken by the CCD camera when the contact area of the drop was expanding or shrinking. The drop images were then analyzed to extract the contact angle information. The contact angles of the drops with expanding contact areas were considered to be the measurements for the advancing contact angle whereas the contact angles corresponding to the shrinking contact areas were the measurements for the receding contact angle.

The properties of the ink are summarized in Table 2.1.

The volume of a single droplet was measured by first weighing a piece of aluminum foil on the microbalance. Then a known number of droplets (typically on the order of 10^5 droplets) were deposited onto the foil. After the drops completely evaporated, the foil was weighed again on the microbalance. The difference between the two weight

Table 2.1. Fluid properties of the ink used in this study.

Ink properties	Values
Molar mass of $Pd(SC_{16}H_{35})_2$, M (g/mol)	625.45
Molar concentration, C (mM)	32
Density, ρ (kg/m^3)	853.99
Surface tension @ 25 °C, σ (mN/m)	24.312
Viscosity, μ $(mPa \cdot s)$	0.602 - 0.603
Advancing contact angle on SiO2/Si, θ_a (°)	13.7 ± 1.9
Receding contact angle on SiO2/Si, θ_r (°)	9.6 ± 1.7

measurements is simply the mass of the deposited drops after complete evaporation. The volume of a single droplet V_0 was then found by

$$V_0 = \frac{m_d}{CMN_d}, \tag{2.1}$$

where m_d is the mass of the deposited drops after complete evaporation, N_d is the number of deposited droplets. In this way the volume of a single droplet V_0 was found to be about 45 pL, corresponding to the in-flight droplet diameter $D_i = 44$ μm.

The speed of the droplet as it was ejected from a nozzle was measured using a novel method without utilizing a high-speed camera (see Appendix A). The ejection speed v_e was found about 5.03 m/s.

3. RESULTS AND DISCUSSIONS

3.1 Drop Time Evolution on a Dry Smooth Solid Surface

3.1.1 Drop Impact, Spreading and Wetting

After a droplet is ejected from a nozzle and then collides with a dry smooth solid surface, it goes through a complex process before it reaches an equilibrium state. R. Rioboo [22] characterized this process with four consecutive phases, namely kinematic phase, spreading phase, relaxation phase and wetting phase. The first two phases strongly depend on the droplet impact parameters. Therefore some researchers combine the first two phases into one phase known as the impact phase [23]. At the end of the impact phase, the drop spreads to its maximum diameter. In the next relaxation phase, the drop experiences either contact angle hysteresis or oscillation and retraction. After that, the deposited drop may continue to spread due to the wetting of the surface [23]. The entire phases of a drop after collision with a solid surface are illustrated in Figure 3.1.

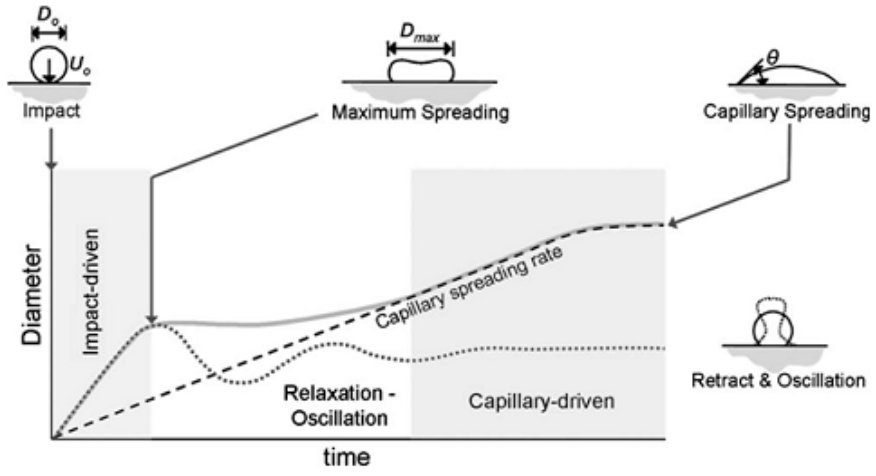

Figure 3.1. Typical drop phases after collision with a solid surface by Hsiao [23].

The time required for a droplet to spread to its maximum diameter D_m (i.e. the time duration of the impact phase) was estimated by $8D_i/3v_e = 23.3$ μs [24]. The maximum spreading factor defined as D_m/D_i was estimated between 2.37 and 2.45 [21]. For typical drop-on-demand inkjet printing conditions, the relaxation phase lasted about 70 - 100 μs [23]. During the wetting phase, the time evolution of the drop diameter was governed by Tanner's power law: $D(t) \propto t^{0.1}$ [25], based on which the time corresponding to the wetting phase was found no larger than 0.63 ms (see Appendix B). Therefore the total time required for a droplet to reach its equilibrium state was less than 0.8 ms.

3.1.2 Drop at the Equilibrium State

Since the Bond number defined as $Bo = \rho g D_i^2/\sigma = 6.67 \times 10^{-4} \ll 1$, the influence of the gravity was negligible compared to the surface tension. Therefore at the equilibrium state the drop formed a spherical cap. The drop volume at the equilibrium state V_{eq} was given by

$$V_{eq} = \frac{\pi(1-\cos(\theta_e))^2(2+\cos(\theta_e))}{24(\sin(\theta_e))^3} D_{eq}^3 = K D_{eq}^3, \tag{3.1}$$

where D_{eq} and θ_e were respectively the drop diameter and the contact angle at the equilibrium state. The equilibrium contact angle θ_e was completely dependent on the properties of the ink and the substrate thus was constant during the inkjet printing. K was the drop volume proportionality constant.

3.1.3 Drop Evaporation

Drop evolution after the equilibrium state is mainly driven by drop evaporation. On an ideal surface, the contact angle is uniquely determined by Equation 1.1 therefore as evaporation proceeds, the contact area of the drop shrinks at a constant contact angle. However, due to the presence of the contact angle hysteresis for the ink and substrate system used in this study, the contact line of the drop would stay pinned

during evaporation until the contact angle decreased from the equilibrium contact angle to the receding contact angle. In order to maintain a pinned contact line, a capillary flow from the main drop had to constantly replenish the evaporation loss from the drop edge. The resulting outward flow carried the dispersed material (i.e. the solute) to the edge [26]. Therefore the concentration of the solute at the edge of the drop became much greater than the concentration of the main drop. Because the solvent used in this study was volatile and among all the areas on a drop surface the evaporation rate at the edge was the largest [26], the liquid at the edge soon reached the saturation concentration and the solute started to precipitate out of the solution, leaving a permanent solid ring deposit along the pinned contact line. When the contact angle was about to decrease below the receding contact angle, the contact line of the drop began to recede. The contact area continuously shrunk as the contact line was receding. After the drop completely evaporated, a circular solid deposit was formed within the drop. The entire drop evolution after collision on the solid substrate is illustrated in Figure 3.2 (a). Figure 3.2 (b) shows the ring deposit and the circular deposit within a drop after the drop completely evaporates. The drop diameter after complete evaporation (i.e the size of the ring deposit) D_0 was found about 125 μm.

Based on the drop evolution process it's obvious that

$$D_{eq} = D_0. \tag{3.2}$$

As it will be shown in the latter sections, the time for a droplet to reach equilibrium (< 0.8 ms) is much smaller than the drop evaporation time. Therefore the evaporation loss before the drop reaches equilibrium state is negligible. The drop volume at the equilibrium state V_{eq} can be approximated by the volume of a single droplet prior to impact V_0. Mathematically this means

$$V_{eq} = V_0. \tag{3.3}$$

Substituting Equation 3.2 and Equation 3.3 into Equation 3.1, we have

$$V_0 = \frac{\pi(1-\cos(\theta_e))^2(2+\cos(\theta_e))}{24(\sin(\theta_e))^3} D_0^3 = K D_0^3. \tag{3.4}$$

Substituting $V_0 = 45$ pL , $D_0 = 125$ μm into Equation 3.4 and solving the equation, the equilibrium contact angle θ_e is about 13.3 ° and the constant K is 0.023.

3.2 Single-layer Printed Line Morphologies

To print a continuous line, a series of equidistant drops are deposited sequentially in a row such that the adjacent drops are overlapped. Two parameters are used to characterize this printing process. The first parameter is the dot spacing defined as the distance between adjacent drops. The second parameter is the time between depositions of adjacent drops, which can be controlled by adjusting the stage scanning speed given specific dot spacing.

By varying the dot spacing from 20 μm to 100 μm and changing the time between depositions of adjacent drops from 2 ms to 350 ms, different morphologies of single-layer lines were obtained. Figure 3.3 shows the lines printed with different time between adjacent drops when the dot spacing is kept fixed at 70 μm. All the lines shown in Figure 3.3 were printed from left to right with respect to the substrate. The lengths of all the lines were about 3 mm.

Based on distinct characteristics, the morphologies of single-layer printed lines are classified into three categories as the time between adjacent drops increases:

(i) one or several agglomerations in the middle of the line with short time between adjacent drops ($<\sim$ 50 ms) as shown in Figure 3.3 (a) and Figure 3.3 (b);

(ii) one agglomeration at the end of the printed line with perceptible ring formations across the line when the time between adjacent drops is medium ($\sim$ 50 ms to $\sim$ 250 ms) shown in Figure 3.3 (c) - (f);

(iii) no perceptible agglomeration with long time between adjacent drops ($>\sim$ 250 ms) shown in Figure 3.3 (g).

Figure 3.4 shows the lines printed with different time between adjacent drops when the dot spacing is 40 μm or 100 μm. Experiments have shown that the above

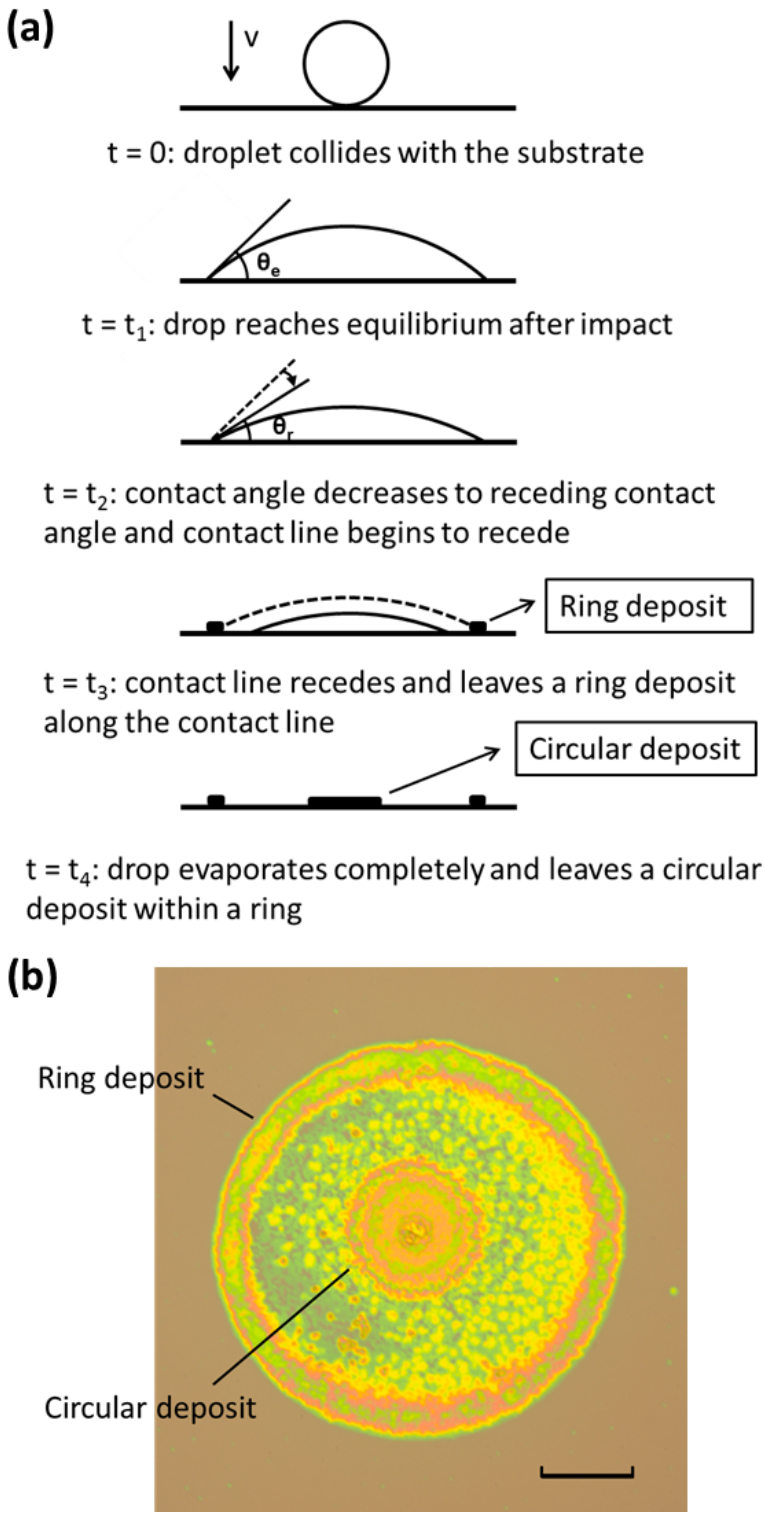

Figure 3.2. (a) Illustration of drop time evolution after collision with the substrate in the presence of contact angle hysteresis and non-zero receding contact angle. (b) A single drop after complete evaporation. The calibration bar represents 30 μm.

classification of printed line morphologies based on the time between adjacent drops is generally appropriate regardless of the dot spacing.

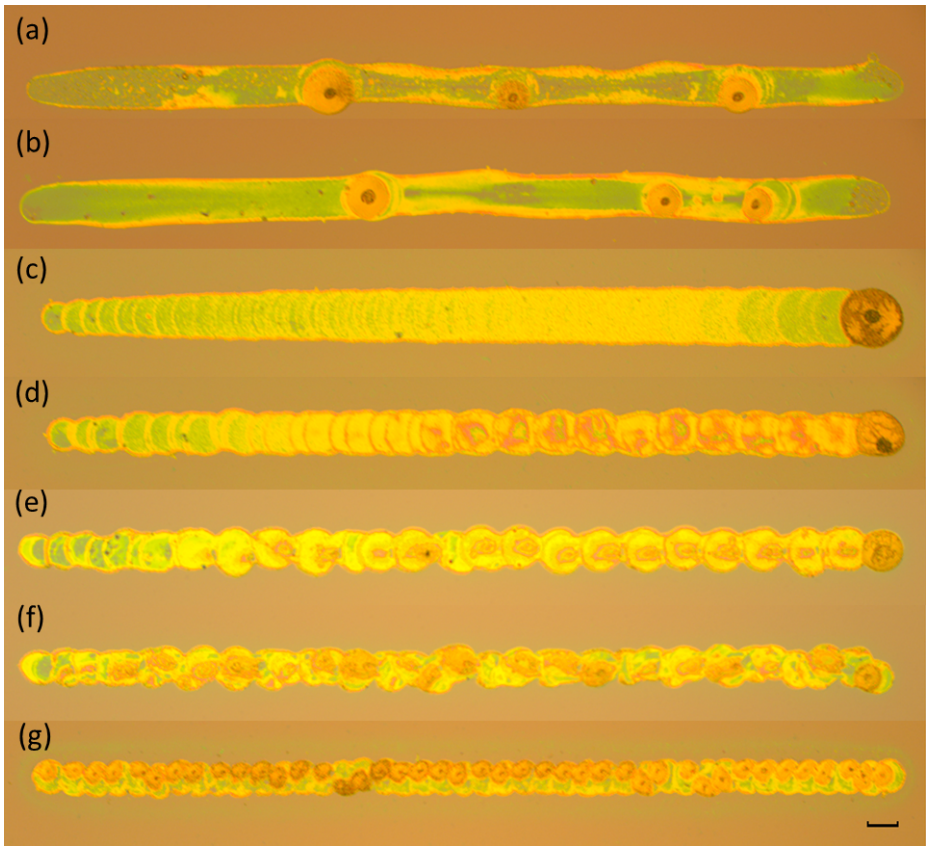

Figure 3.3. Single-layer lines printed from left to right with dot spacing 70 μm, time between adjacent drops (a) 2 ms; (b) 10 ms; (c) 70 ms; (d) 100 ms; (e) 150 ms; (f) 200 ms; (g) 290 ms. The lengths of all the lines are about 3 mm. The calibration bar represents 100 μm.

3.2.1 Single-Layer Line Morphologies with Short or Medium Time between Adjacent Drops

To gain more insights into the line morphologies with short or medium time between adjacent drops, I printed lines with different lengths while keeping dot spacing and time between adjacent drops fixed (Figure 3.5). With short time between adja-

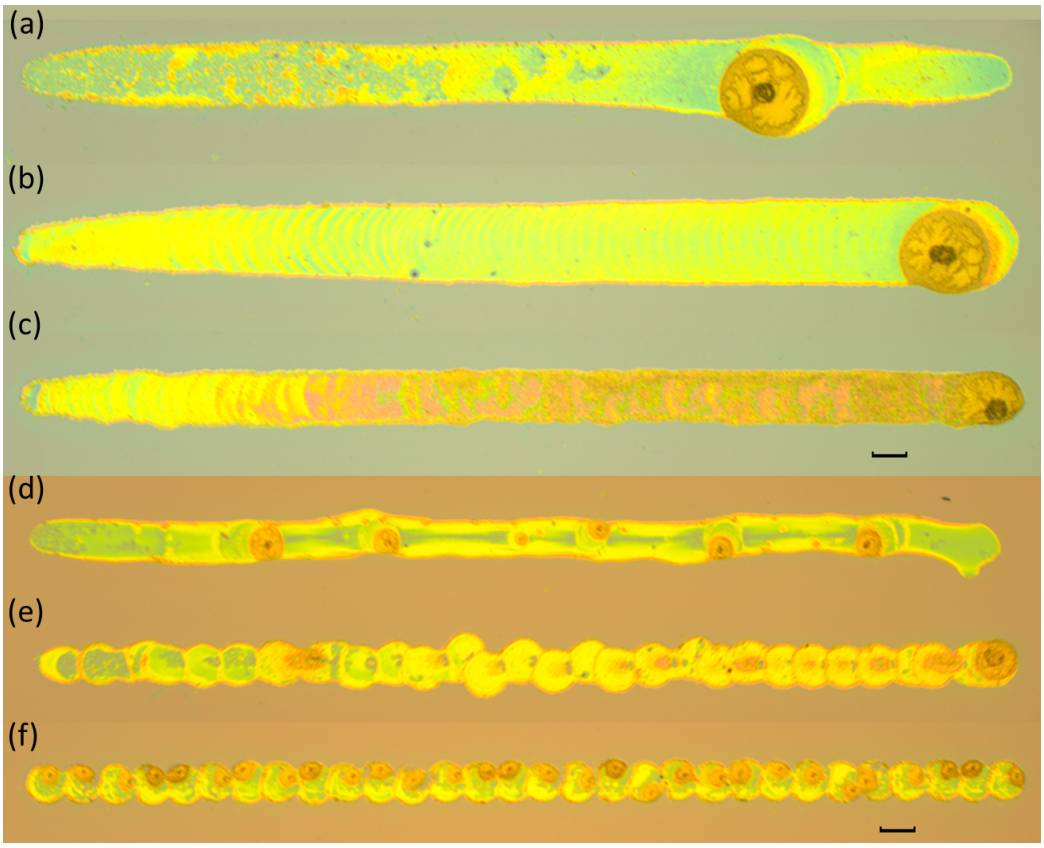

Figure 3.4. Single-layer lines printed from left to right with dot spacing and time between adjacent drops (a) 40 μm, 5 ms; (b) 40 μm, 50 ms; (c) 40 μm, 100 ms; (d) 100 μm, 5 ms; (e) 100 μm, 150 ms; (f) 100 μm, 350 ms. The lengths of all the lines are about 3 mm. The calibration bars represent 100 μm.

cent drops (Figure 3.5 (a)), the number and the location of agglomerations within a line varied with the length of the printed line whereas with medium time between adjacent drops (Figure 3.5 (b)), only one agglomeration existed and was always situated at the end of the printed line regardless of the length of the line. It's worth pointing out that the location of the agglomeration with medium time between adjacent drops only depended on the direction of printing. This was confirmed by the observation of an agglomeration at the left end of a line when the line was printed from right to left. Therefore the possibility that the agglomeration was formed due to a tilted surface of the substrate was eliminated. Apparently when the line was printed with medium time between adjacent drops, ink tended to migrate to the end where the last drop was deposited.

3.2.2 Single-Layer Line Morphologies with Long Time between Adjacent Drops

When a line was printed with long time between adjacent drops (Figure 3.3 (g), Figure 3.4 (f)), the line width was always about the diameter of a single drop. Further increasing the time between adjacent drops did not make essential changes in the printed line morphology. Separate single drops could be distinguished within a line when the dot spacing was larger than the half of drop diameter. Based on these observations I concluded that during the long time period between adjacent drops, a very large portion of the deposited drop must have evaporated prior to making contact with the next arriving droplet so that the interactions between adjacent drops were minimal. Simulation has shown that more than 99% of the drop is lost due to evaporation during the initial time period of 250 ms, which was the smallest long time between adjacent drops [21]. Effectively we can consider printing a line with long time between adjacent drops is a process in which every deposition takes place when the previously deposited drops are dry.

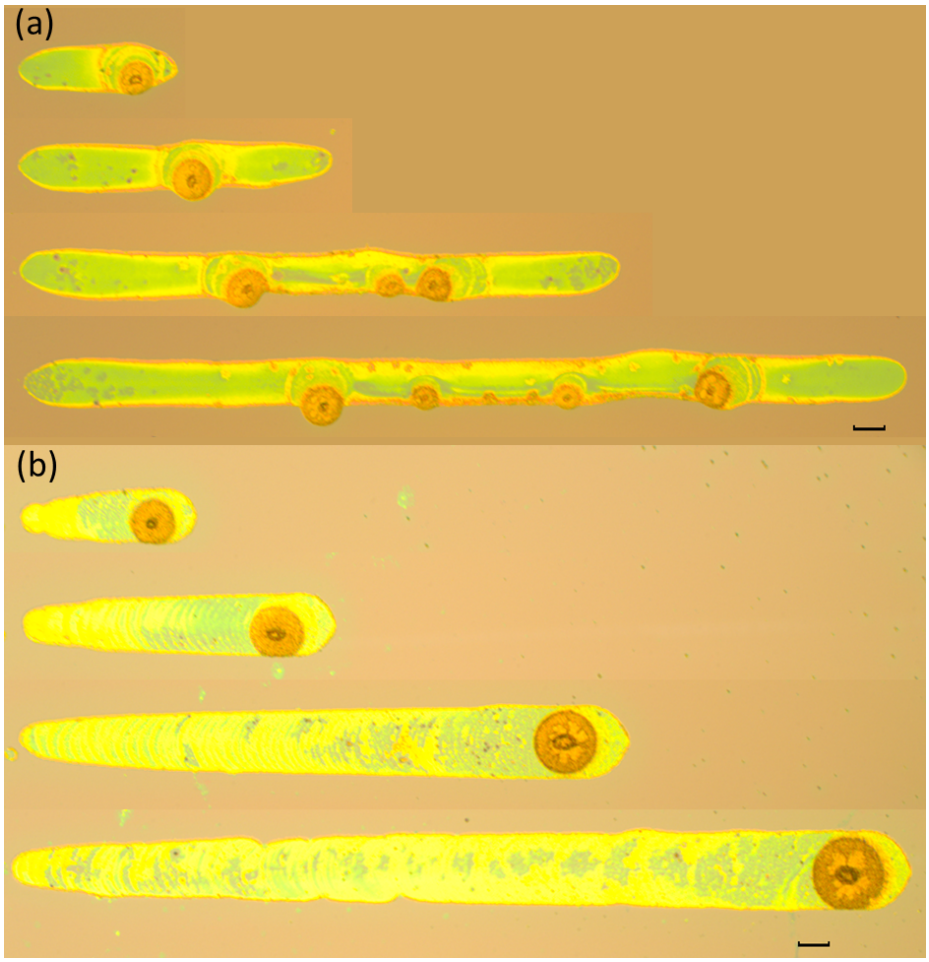

Figure 3.5. Single-layer lines printed from left to right with different lengths (a) dot spacing = 70 μm, time between adjacent drops = 5 ms; (b) dot spacing = 40 μm, time between adjacent drops = 50 ms. In each figure, the lengths of the lines from the top to the bottom are 0.5 mm, 1 mm, 2 mm and 3 mm. The calibration bar represents 100 μm.

3.3 Fluid Explanation of Printed Line Morphologies

3.3.1 Explanation of Ink Migration with Medium Time between Adjacent Drops

The time for a drop to reach its equilibrium state (< 0.8 ms) was much smaller than the medium time between adjacent drops (> 50 ms). Therefore when the second droplet impacted onto the first drop on the substrate, the first drop had already equilibrated. In addition, it had lost a considerable amount of volume due to the evaporation of the volatile solvent.

To validate this argument, a simple and conservative estimation of the evaporation loss during the medium time between adjacent drops is performed. As discussed in the previous section, more than 99% of the drop evaporated during initial 250 ms. Even the smallest medium time between adjacent drops (~ 50 ms) is equivalently about 20% of this amount of time. Moreover, the evaporation rate of a drop on the surface decreases towards the end of evaporation process [21, 27]. This implies that the actual evaporation loss during the initial time period of 50 ms is greater than 20% of the volume of a single drop. Therefore the molar concentration (defined as the moles of the solute divided by the volume of the solution) of the first drop considerably increased when the second drop arrived.

It is well known that a change in the molar concentration of a solution results in a change in the surface tension [28]. The dependence of the surface tension on the molar concentration for a specific solution can be determined using Gibbs Adsorption Equation [29]:

$$d\gamma = -\sum_i \Gamma_i d\mu_i, \tag{3.5}$$

where γ is the surface tension of a liquid, Γ_i and μ_i are respectively the surface excess and the chemical potential of the component i. For a surface located between two phases: α phase and β phase, the surface excess Γ_i is defined by

$$\Gamma_i = \frac{n_i^{TOTAL} - n_i^{\alpha} - n_i^{\beta}}{A_s}, \tag{3.6}$$

where n_i^{TOTAL} is the total moles of the i^{th} component in the surface system. n_i^{α} and n_i^{β} are respectively the moles of the i^{th} component in the α and β phase. A_s is the area of the dividing surface. The chemical potential of the i^{th} component is linearly dependent on the natural logarithm of the concentration.

For a two-component solution used in this study, whether the surface tension increases with the molar concentration is completely dependent on the tendency of the solute to accumulate near the liquid surface or move into the bulk. This tendency is indicated by the sign of the surface excess of the solute in Equation 3.5. If the surface excess of the solute is positive, which means that the solute tends to accumulate near the liquid surface, the surface tension of the solution decreases as the molar concentration increases. Conversely, if the surface excess is negative, the surface tension increases with the molar concentration.

The surface tension of the ink ($24.312\ mN/m$) was measured to be smaller than the surface tension of pure toluene ($27.73\ mN/m$ [30]), of which the molar concentration is zero. This indicates that the surface excess of the solute must be positive. In other words, the surface tension of the ink decreases as the molar concentration increases.

Therefore when the second drop began to merge with the first drop, the second drop had higher surface tension than the first drop. A flow induced by this surface tension gradient pulled the first drop towards the second drop. In fact Duineveld used this concentration-induced surface tension gradient to validate his model assumption of negligible ink evaporation during the course of printing [16].

After the first two drops merged and equilibrated, the merged drop continued to evaporate before it made contact with the third upcoming drop. Since the merged drop had higher molar concentration thus smaller surface tension than the third drop, the third drop pulled the merged drop to its side. The later deposited drops followed this process and kept dragging the liquid bead on the substrate. Once the printing was finished, the bead evaporated completely, leaving a dense agglomeration at the end of the printed line.

Another essential fact that contributed to the ink migration was that the medium time between adjacent drops was actually long enough so that the liquid bead on the substrate had depinned from its initial contact line prior to merging with the next arriving droplet. One of the signs that a bead has already depinned from its contact line is the ring formation along the contact line and there are noticeable drop ring formations in the lines printed with medium time between adjacent drops (Figure 3.3 (c) - (f), Figure 3.4 (b), (c), Figure 3.5 (b)). A bead with a moving contact line had low pinning forces on the solid surface thus facilitating the hydrodynamic pulling by the adjacent drop.

3.3.2 Explanation of Printed Line Morphologies with Medium Time between Adjacent Drops

From the discussions in the previous section, we can see that printing a line with medium time between adjacent drops is essentially the process in which the deposited droplets consistently pull and merge with the liquid bead on the substrate. The volume of the liquid bead after every deposition directly determines the size of the ring formation. Therefore we can understand how the ring size changes across a line through the analysis of the bead volume.

Bead Volume Analysis

To facilitate the formulation of the bead volume after every deposition, some assumptions and simplifications are made:

- Negligible time for a drop to reach its equilibrium state after collision with the substrate. The time for a drop to reach equilibrium is less than 0.8 ms, which is two orders of magnitude smaller than the smallest medium time between adjacent drops ($\sim$ 50 ms).

- Negligible time for a liquid bead on the substrate to merge with the next arriving droplet upon contact. The time scale of the merging event can be estimated by $0.5(\rho D_i^3/\sigma)^{0.5} = 27.4\ \mu s$ [31], which is much smaller than the time between adjacent drops.

- Deposited droplets are ideal solutions. Therefore the volume of the bead and the volume of the arriving droplet can be directly added when they merge.

- Droplets leave the nozzle with constant volume.

Figure 3.6 (a) illustrates the time evolution of the liquid bead on the substrate during the first three depositions. Superscript + and - are only used to show the sequence of the events with - representing an event that occurs just before an instant and + representing an event just after an instant. Effectively we can consider the two events with superscript + and - happen simultaneously following the first two simplifications. At t = 0, the first drop collides with the substrate and reaches equilibrium with contact angle θ_e. After one period of time between adjacent drops (i.e. at t = τ), the second drop arrives when the first drop has depinned and a solid ring deposit has been formed along its initial contact line. The two drops quickly merge upon contact and equilibrate to a spherical cap with contact angle θ_e. Similar analysis can be performed to the later depositions. After a line is printed, a chain of overlapped drop ring deposits are formed within a line. Figure 3.6 (b) shows the ring formations within a line printed with medium time between adjacent drops.

Let's define the bead volume just after the n^{th} deposition (i.e. at t = (n-1)τ^+) V_n. Then we have

$$V_n = nV_0 - \sum_{i=1}^{n-1} \triangle V_{i,i+1} \quad (n = 2, 3, 4...) \tag{3.7}$$

and

$$V_1 = V_0, \tag{3.8}$$

where $\triangle V_{i,i+1}$ is the volumetric loss of the liquid bead due to evaporation from the i^{th} deposition to the $(i+1)^{th}$ deposition (i.e from t = $(i-1)\cdot\tau^+$ to t = $i\cdot\tau^-$). V_0

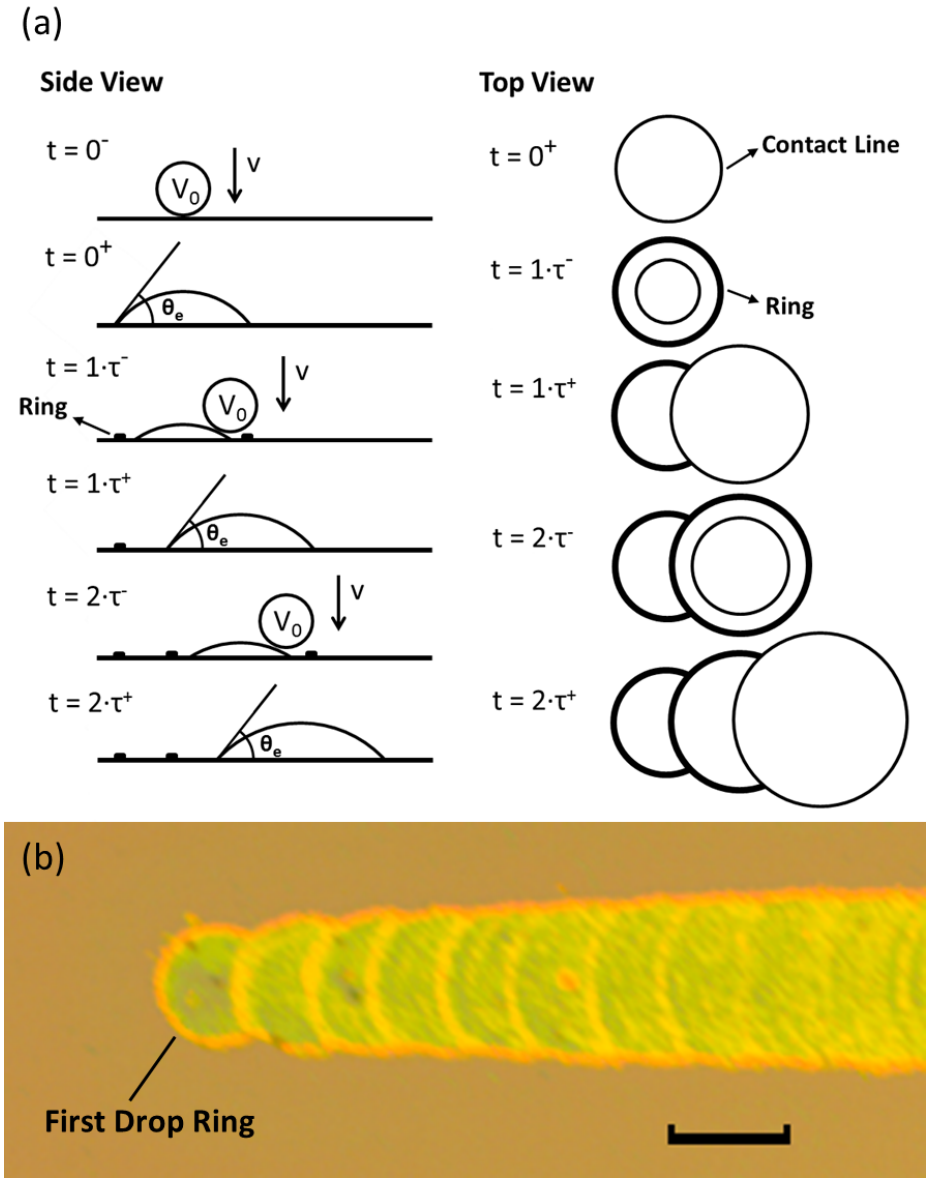

Figure 3.6. (a) Illustration of time evolution of the liquid bead on the substrate when a line is printed with medium time between adjacent drops. τ is the time between adjacent drops. (b) A close-up view of Figure 3.3 (c). A chain of overlapped drop rings are formed in a line. The calibration bar represents 100 μm.

is the droplet volume prior to impact or merging, which has been assumed to be a constant.

Rewrite Equation 3.7 in the form of the 1^{st} order forward difference equation, then we have

$$\triangle V_n = V_{n+1} - V_n = V_0 - \triangle V_{n,n+1} \quad (n \in \mathbb{N}^*). \tag{3.9}$$

$\triangle V_{n,n+1}$ by definition captures the amount of evaporation loss starting from a bead of a spherical cap with volume V_n for an extended period of τ. Therefore $\triangle V_{n,n+1}$ is a function of V_n and τ. So Equation 3.9 becomes

$$\triangle V_n = V_0 - f(V_n, \tau) \quad (n \in \mathbb{N}^*). \tag{3.10}$$

Therefore the 2^{nd} order forward difference of the bead volume $\triangle^2 V_n$ can be expressed as

$$\triangle^2 V_n = \triangle V_{n+1} - \triangle V_n = f(V_n, \tau) - f(V_{n+1}, \tau) \quad (n \in \mathbb{N}^*). \tag{3.11}$$

Previous studies [27, 32] have shown that the evaporation rate increases with the drop base radius. The base radius of the spherical-cap bead is proportional to the bead volume to the power of 1/3 according to Equation 3.1. Hence the evaporation rate increases with the bead volume V_n. Within a printed line the time between adjacent drops τ is fixed. So the amount of evaporation loss $f(V_n, \tau)$ within a line increases with V_n. Therefore if $\triangle V_n > 0$ (i.e. $V_{n+1} > V_n$), $f(V_{n+1}, \tau) > f(V_n, \tau)$. Based on Equation 3.11, we have $\triangle^2 V_n < 0$. Similarly if $\triangle V_n < 0$, $\triangle^2 V_n > 0$. Physically this means that as the number of depositions increases, the bead volume increases or decreases at a decaying rate.

The equilibrium bead volume V_e can be found by enforcing $\triangle V_n = 0$ in Equation 3.10:

$$V_0 = f(V_e, \tau). \tag{3.12}$$

For a line printed with medium time between adjacent drops, the first drop partially evaporates when the second drop arrives. Mathematically it means that $f(V_1, \tau) < V_0$. Using Equation 3.10 we simply have $\triangle V_1 > 0$. Using Equation 3.12,

the inequality becomes $f(V_1, \tau) < f(V_e, \tau)$. Because $f(V_n, \tau)$ increases monotonically with V_n, we have $V_1 < V_e$. As we can see the bead volume V_n increases initially below the equilibrium volume V_e.

If the bead volume $V_n > V_e$, $f(V_n, \tau) > f(V_e, \tau)$. With Equation 3.10 and 3.12, we have $\triangle V_n < 0$. Similarly if $V_n < V_e$, $\triangle V_n > 0$. Therefore the dynamics of the bead volume V_n can be considered as a stable discrete system with equilibrium of V_e.

Now let's investigate the effect of the time between adjacent drops on the dynamics of the bead volume. Physically it's obvious that the evaporation loss $f(V_n, \tau)$ during the time between adjacent drops increases with the amount of the time between adjacent drops τ given the same bead volume V_n. Therefore in order to make Equation 3.12 hold, the equilibrium volume V_e must decrease as τ increases.

Overall, the behavior of the bead volume is summarized as:

When a line is printed with medium time between adjacent drops, the bead volume initially increases with the number of depositions at a decreasing increment before it reaches or oscillates about an equilibrium. The equilibrium volume decreases when the time between adjacent drops increases.

Ring Size Analysis

The bead on the substrate leaves a ring deposit after the contact line recedes as illustrated in Figure 3.6 (a). According to Equation 3.1, the size of the ring formed after the n^{th} deposition D_n and the bead volume V_n are related by

$$V_n = KD_n^3. \tag{3.13}$$

Following the discussions in the previous section, two equations are used to describe the initial increment of the bead volume V_n with the number of depositions n:

$$\triangle V_n > 0 \tag{3.14}$$

and

$$\triangle^2 V_n < 0. \tag{3.15}$$

Substituting Equation 3.13 into Equation 3.14 and using finite difference operation, we have

$$[(\triangle D_n + 1.5D_n \triangle D_n)^2 + 0.75D_n^2] \triangle D_n > 0. \tag{3.16}$$

Obviously the term in the bracket of Equation 3.16 is greater than zero. Therefore $\triangle D_n > 0$, which means the ring size D_n increases with n.

Substituting Equation 3.13 into Equation 3.15 and using finite difference operation, we have

$$\frac{\triangle D_{n+1}}{\triangle D_n} < \frac{D_{n+1}^2 + D_{n+1}D_n + D_n^2}{D_{n+2}^2 + D_{n+2}D_{n+1} + D_{n+1}^2}. \tag{3.17}$$

If $D_{n+2} \geq D_{n+1}$, by observation we have

$$\frac{D_{n+1}^2 + D_{n+1}D_n + D_n^2}{D_{n+2}^2 + D_{n+2}D_{n+1} + D_{n+1}^2} < 1. \tag{3.18}$$

Comparing Equation 3.17 and Equation 3.18, we have $\triangle D_{n+1} < \triangle D_n$ (i.e. $\triangle^2 D_n < 0$). If $D_{n+2} < D_{n+1}$, obviously $\triangle D_{n+1} < 0 < \triangle D_n$. Hence $\triangle^2 D_n < 0$.

In sum, $\triangle^2 D_n < 0$. This means that the increment of the ring size is decreasing.

After the initial increment, the bead volume is either a constant or oscillating about an equilibrium. If the bead volume is constant (i.e. $V_n = V_e = constant$), it's obvious that $D_n = D_e = constant$ using Equation 3.13. If $V_n < V_e$, $KD_n^3 < KD_e^3$ (Equation 3.13). Since D_n^3 is monotonically increasing with D_n, $D_n < D_e$. Similarly if $V_n > V_e$, $D_n > D_e$. Therefore when the bead volume oscillates about an equilibrium the ring size also oscillates about an equilibrium.

Therefore the evolution of the ring size with the number of depositions is predicted as in Figure 3.7, where D_e is the equilibrium ring size given by

$$D_e = (\frac{V_e}{K})^{1/3} \tag{3.19}$$

and D_0 is the diameter of a single drop after evaporation given by

$$D_0 = (\frac{V_0}{K})^{1/3} \tag{3.20}$$

based on Equation 3.4.

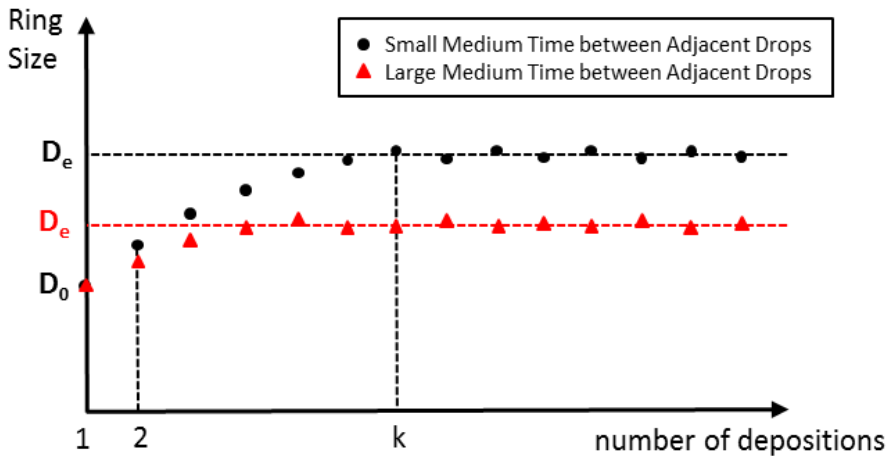

Figure 3.7. Predicted changes of the ring sizes in a line with small and large medium time between adjacent drops. D_e is the equilibrium ring size and D_0 is the single drop diameter.

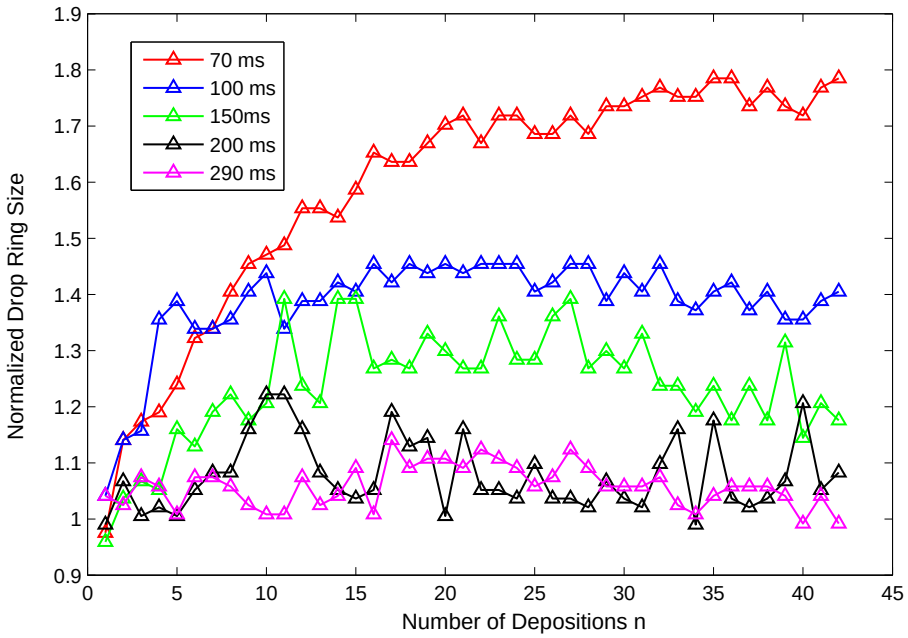

Figure 3.8. Normalization of measured drop ring sizes in a line with different time between adjacent drops when the dot spacing is 70 μm. The drop ring size is normalized with respect to the diameter of a single drop.

Validation of Proposed Explanation

Figure 3.8 shows the normalized drop ring sizes across a line printed with different time between adjacent drops, obtained by processing optical line images in Figure 3.3 (c) - (g). The local peaks of the line width at the vicinity of deposition positions were found through image analysis as good measurement of the drop ring sizes after every deposition. The drop ring size was further normalized with respect to the diameter of a single drop after evaporation.

As we can see, the measured drop ring sizes across a line reasonably agree with the predicted trend in Figure 3.7. The normalized ring size always starts at about 1 ($< \pm 5\%$) for all the printed lines. This supports the prediction in Figure 3.7 that the first ring size is always equal to the diameter of a single drop.

With the drop ring sizes being measured, the bead volume after every deposition was obtained using Equation 3.13. To minimize the effect of the droplet volume uncertainty and noises in the drop ring size measurement on the bead volume data, the obtained bead volumes were processed in MATLAB with a digital low-pass filter prior to further analysis. Figure 3.9 shows the bead volume after every deposition with and without filtering for the line printed with 70 μm dot spacing and 70 ms between adjacent drops.

Based on the filtered bead volumes, the evaporation loss between any adjacent depositions $f(V_n, \tau)$ could be found using Equation 3.8 and Equation 3.10. Figure 3.10 and Figure 3.11 show the bead volumes as a function of number of depositions n and the bead volume V_n respectively.

The bead volume is predicted to have decreasing increment at the beginning and then stay constant or oscillate about an equilibrium after a certain deposition. With Equation 3.10, the evaporation loss $f(V_n, \tau)$ is predicted accordingly to have initial increment at the beginning before reaching or oscillating about the equilibrium of a single droplet volume, which has been experimentally found out to be about 45 pL. This prediction reasonably agrees with the evaporation loss as shown in Figure 3.10.

Another prediction that the evaporation loss monotonically increases with the bead volume V_n is fairly well supported by Figure 3.11.

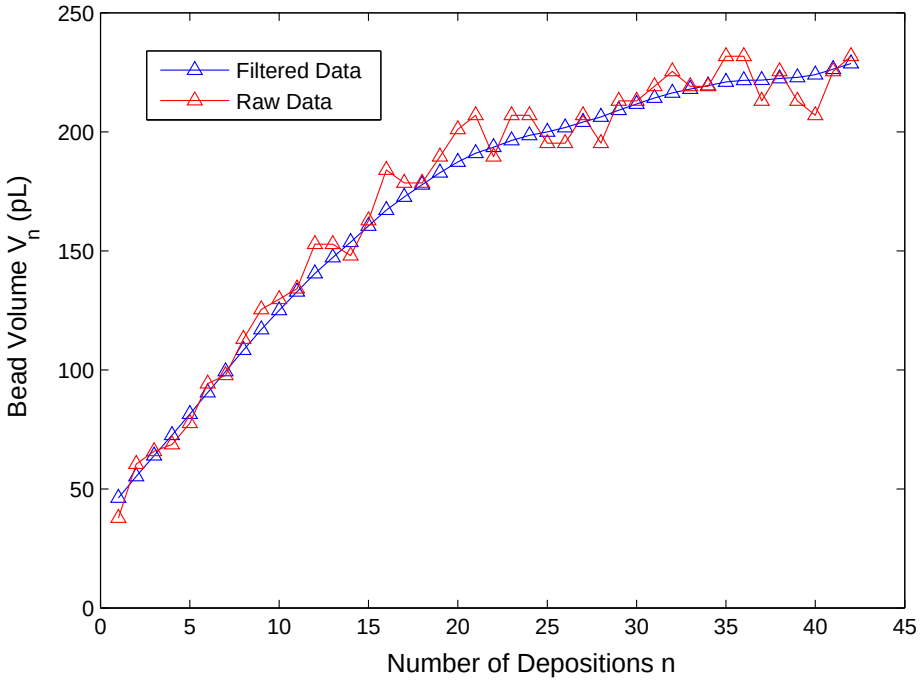

Figure 3.9. Changes of the bead volumes with the number of depositions when the dot spacing and the time between adjacent drops are respectively 70 μm and 70 ms. The raw bead volumes are obtained directly from the measured drop ring sizes for the line in Figure 3.3 (c). The raw bead volumes are further processed with a digital low-pass filter.

3.3.3 Explanation of Printed Line Morphologies with Long Time between Adjacent Drops

As we've discussed earlier, when a line is printed with long time between adjacent drops, every deposited drop can be considered to have evaporated completely prior to the arrival of the next droplet. Therefore the volumetric loss due to evap-

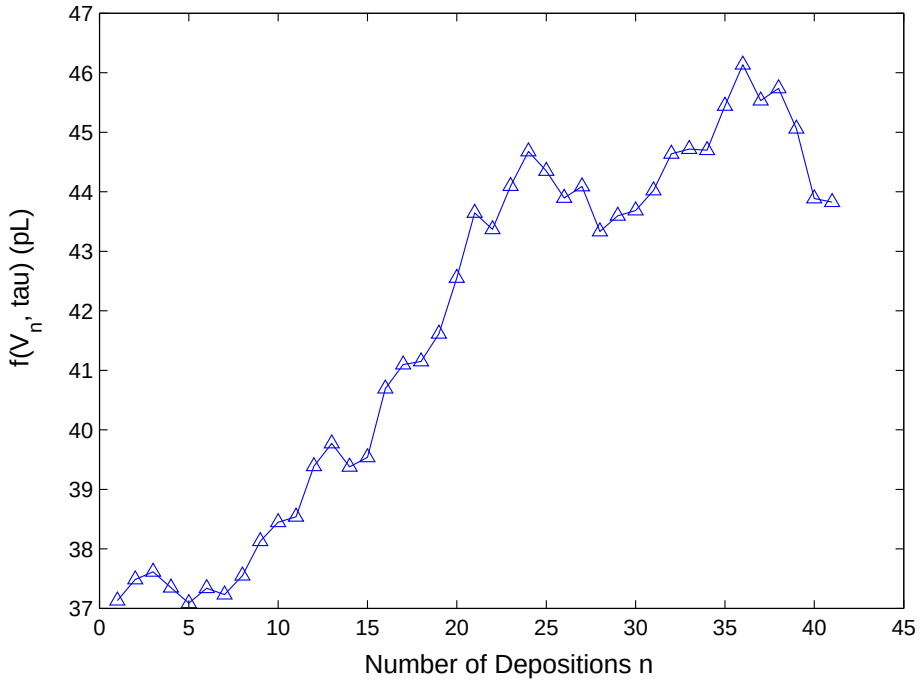

Figure 3.10. Evaporation loss of the bead volume between adjacent depositions as a function of the number of depositions for the line printed with dot spacing 70 μm and 70 ms between adjacent drops.

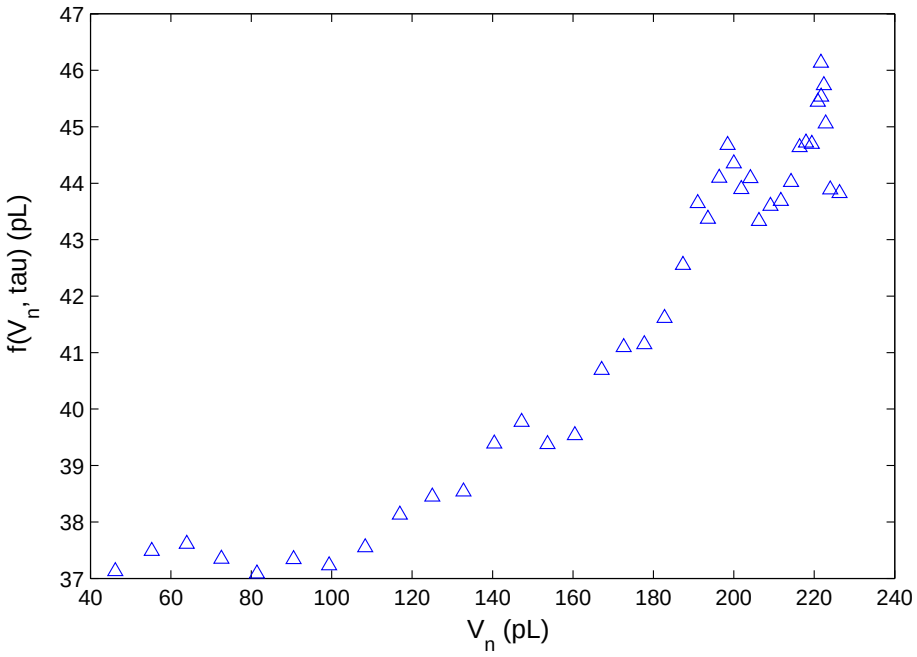

Figure 3.11. Evaporation loss of the bead volume between adjacent depositions as a function of the bead volume for the line printed with dot spacing 70 μm and 70 ms between adjacent drops.

oration during the time between adjacent drops is equal to a single droplet volume. Mathematically this means

$$\triangle V_{n,n+1} = V_0 \quad (n \in \mathbb{N}^*). \tag{3.21}$$

Substituting Equation 3.21 into Equation 3.9, we have

$$V_{n+1} = V_n \quad (n \in \mathbb{N}^*). \tag{3.22}$$

Using Equation 3.8 and Equation 3.22, we simply get

$$V_n = V_0 \quad (n \in \mathbb{N}^*). \tag{3.23}$$

With Equation 3.13, Equation 3.20 and Equation 3.23, we have

$$D_n = D_0 \quad (n \in \mathbb{N}^*). \tag{3.24}$$

What Equation 3.24 states is that the ring size across a printed line D_n is a constant equal to the diameter of a single drop. In other words, the normalized drop ring sizes are always equal to 1 across a printed line. This reasonably agrees with the measured ring sizes in a line printed with 290 ms between adjacent drops (magenta line in Figure 3.8).

3.3.4 Explanation of Printed Line Morphologies with Short Time between Adjacent Drops

When a line is printed with short time between adjacent drops, the first drop merges with the second drop while its contact line is still pinned (i.e. the contact angle is still larger than the receding contact angle). The evaporation loss during the time between adjacent drops is small because of the short time between adjacent drops. As a result, the surface tension gradient due to changes in molar concentration is weak. Therefore the ink migration with short time between adjacent drops is not as strong as that with medium time between adjacent drops.

The agglomerations in the middle of a printed line (Figure 3.3 (a), (b), Figure 3.5 (a) and Figure 3.4 (a), (d)) are believed to be a result of complex competing dynamics between the pulling forces due to the surface tension gradient and time-varying pinning conditions of the contact line of the liquid bead on the substrate. However, the exact fluid dynamics that leads to the formation of those agglomerations is still unclear at the moment and requires further investigation.

3.4 Multi-layer Printed Line Morphologies

It is important to study the morphologies of multi-layer printed lines because increasing the number of print layers is an effective method to reduce the line resistance and improve the fidelity of the printed line [33–36]. It has been shown that the morphology of a multi-layer line has strong correlations with the electrical conductivity of the line [19, 37].

3.4.1 Multi-layer Line Morphologies with Short or Medium Time between Adjacent Drops

Figure 3.12 shows the multi-layer line morphologies with short or medium time between adjacent drops when all the lines were overprinted 15 times with dot spacing 40 μm. All the layers were printed in the same direction from left to right. Sufficient time was allowed between depositions of successive layers so that the previous layer was completely dry before a new layer was deposited.

When each layer was printed with short time between adjacent drops (Figure 3.12 (a)), the line morphology appeared to be highly irregular with several perceptible agglomerations in the middle of the line. These agglomerations could be considered as the accumulation of agglomerations in each layer.

When each layer was printed with medium time between adjacent drops (Figure 3.12 (b) - (f)), a dense agglomeration, shown as dark brown color in the figures,

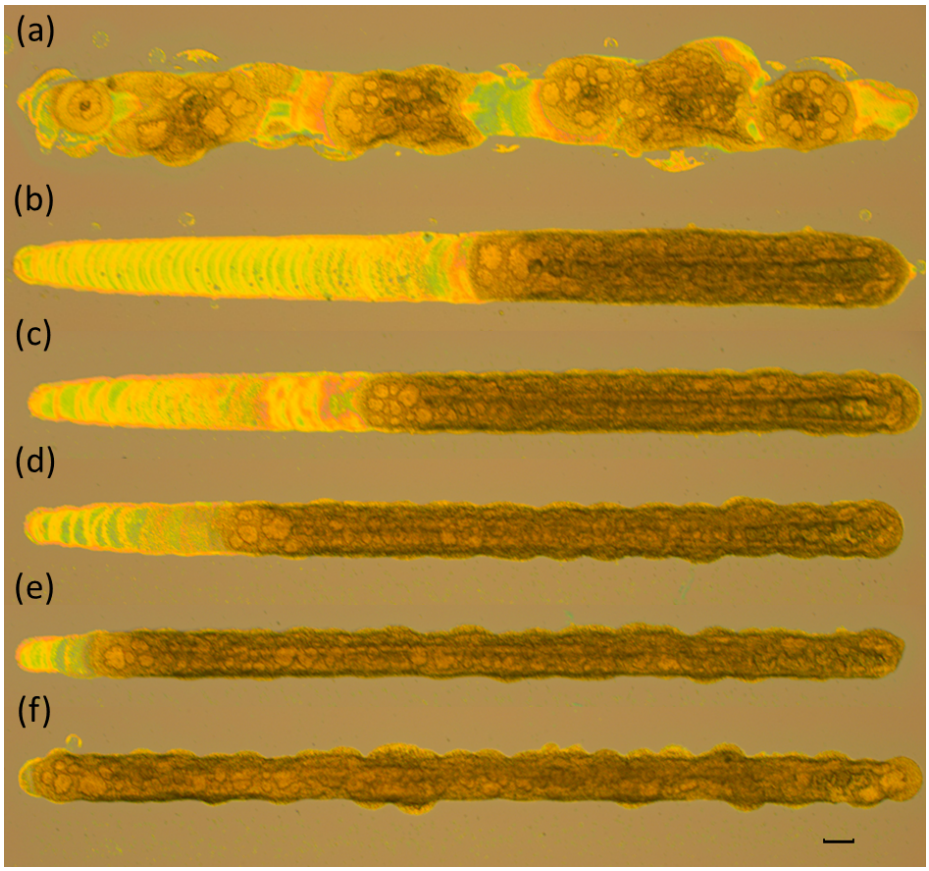

Figure 3.12. 15-layer lines printed unidirectionally from left to right with dot spacing 40 μm, time between adjacent drops (a) 10 ms; (b) 110 ms; (c) 130 ms; (d) 150 ms; (e) 170 ms; (f) 190 ms. The lengths of all the lines are about 3 mm. The calibration bar represents 100 μm.

was observed at the end of the line. This could be understood by considering the cumulative effect of ink migration that took place in every layer.

As the time between adjacent drops increased, the length of the agglomeration grew. This was because larger time between adjacent drops resulted in greater evaporation loss in the liquid bead thus less amount of the wet bead participated in the ink migration process. Therefore the degree to which ink migration occurred in each layer decreased as the time between adjacent drops increased. Image analysis further revealed that the length of agglomeration increased linearly with the time between adjacent drops as shown in Figure 3.13.

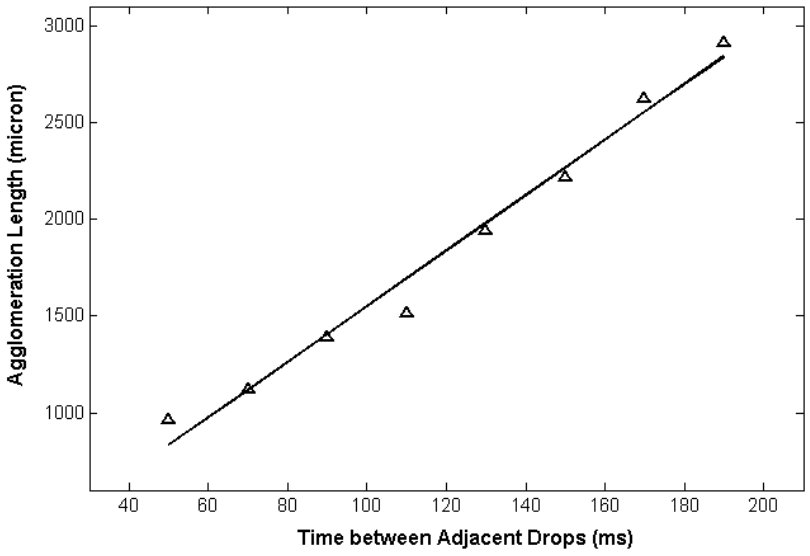

Figure 3.13. Length of agglomeration increased linearly with the time between adjacent drops when a 15-layer line was printed unidirectionally with dot spacing 40 μm. Linear regression (black line) fit the measured lengths (triangles) with coefficient R^2 of 0.98.

3.4.2 Multi-layer Line Morphologies with Long Time between Adjacent Drops

Figure 3.14 (a) shows the lines printed with different number of layers when the dot spacing and the time between adjacent drops were 40 μm and 290 ms respectively. All the layers were printed unidirectionally from left to right.

The beginning of the printed line appeared to be darker than the end of the line. This trend became more and more profound as the number of layers increased. This unbalanced color intensity across a printed line well indicated a non-uniform material distribution across a line. To be more specific, the darker region consisted of more materials. This suggested that there was some ink migration to the beginning of a multi-layer line when the line was unidirectionally printed with long time between adjacent drops. Interestingly enough, the direction of this ink migration was opposite to that of the ink migration when a line was printed with medium time between adjacent drops.

3.4.3 Explanation of Multi-layer Line Morphologies with Long Time between Adjacent Drops

When a droplet is deposited onto the bulk layer that has been previously laid down, unlike the case of a single-layer printed line where there is no mass exchange between the droplet and the solid surface, it dissolves the bulk layer because the bulk layer shares the same solvent with the droplet. This dissolution process lasts the entire life of the drop. After the drop completely evaporates, a crater-like hole is typically formed in the bulk layer [38–40] as shown in Figure 3.15. Since each layer is printed with long time between adjacent drops, the first drop has finished evaporation and dissolution process prior to the arrival of the second droplet. When the second drop lands on the bulk layer, part of the drop falls and slips into the hole created by the first drop due to gravity. The second drop then 'eats' the bulk layer underneath as the evaporation progresses thus making the hole even wider and deeper. Similar

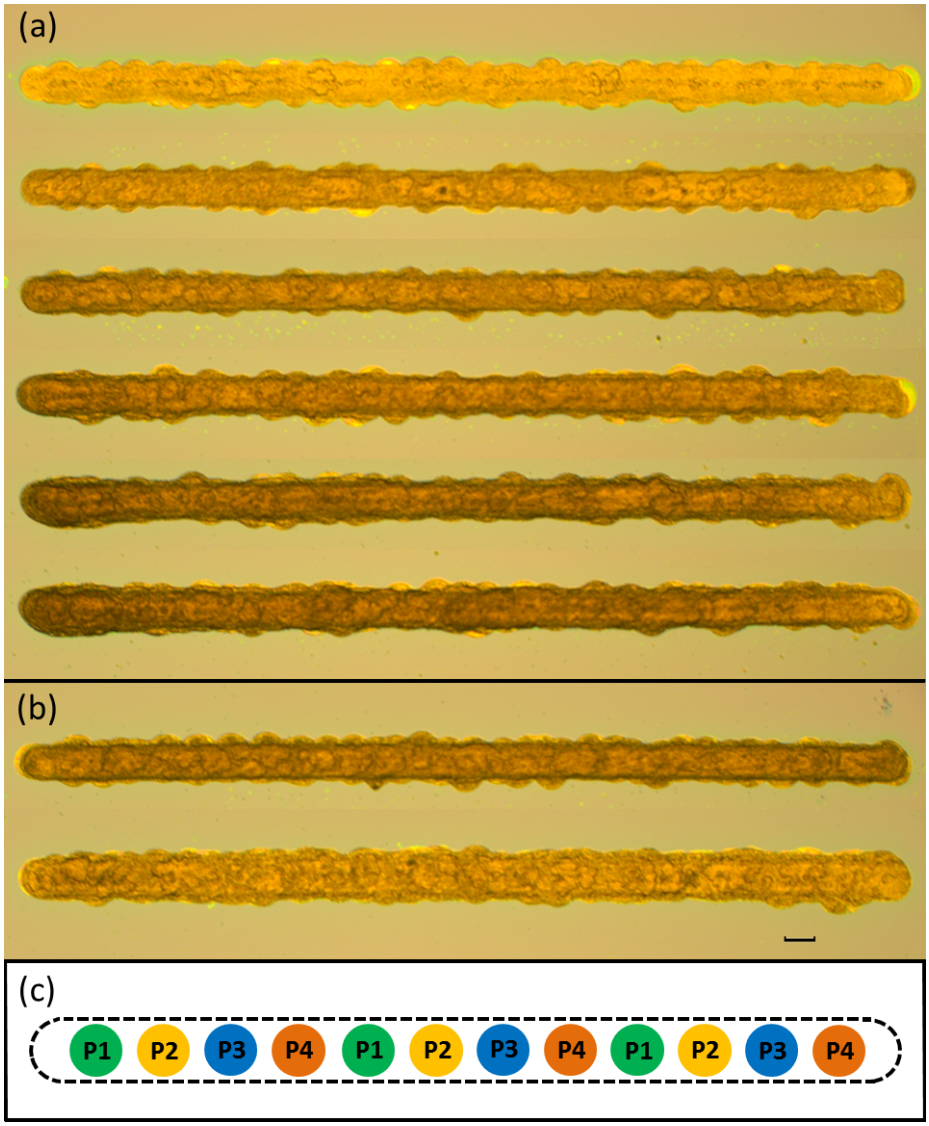

Figure 3.14. (a) Multi-layer lines printed unidirectionally from left to right with dot spacing 40 μm, 290 ms between adjacent drops. The numbers of layers from the top line to the bottom line were 3, 5, 7, 10, 13 and 15. (b) Two 10-layer lines with dot spacing 40 μm. The first line was printed bidirectionally with 290 ms between adjacent drops. The second line was printed with 5 passes. The lengths of all the lines were about 3 mm. The calibration bar represents 100 μm. (c) Illustration of a 4-pass printing routine for a line. Drops in a line are deposited in 4 passes in the sequence of P1, P2, P3 and P4.

process will be repeated for the third and the fourth drop and so forth, as shown in Figure 3.16 (a).

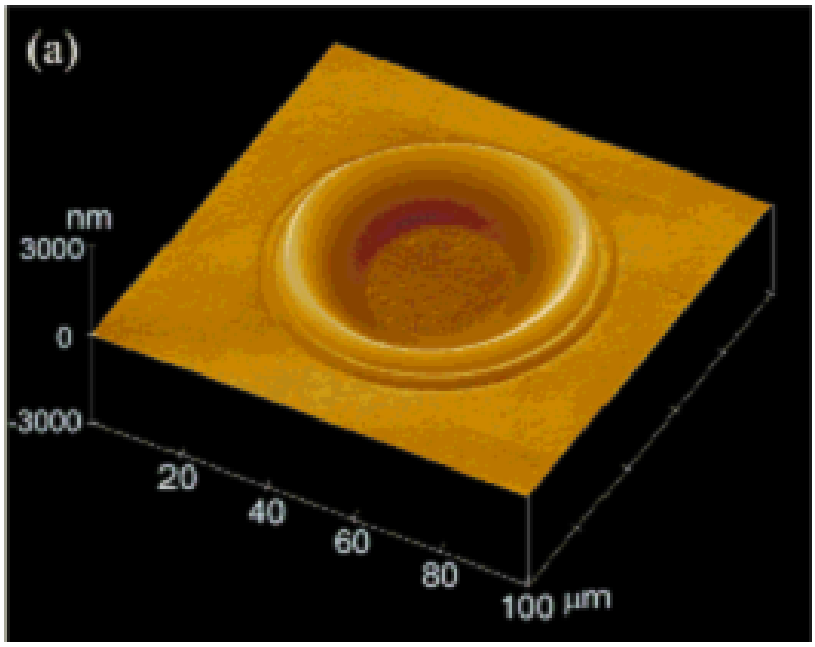

Figure 3.15. A crater hole is typically formed after a drop dissolves the bulk layer and evaporates by Kawase [38].

After a full layer is deposited, the printed line has more material at the beginning than the end because of the ink migration through the slip motion of the liquid into the hole. Furthermore, the beginning of the layer profile is the shallowest. This inclined profile facilitates the slip motion of the liquid in the next deposited layer provided that the next layer is printed in the same direction as the current layer. Therefore the extent to which the ink migrates to the beginning grows as the number of unidirectionally printed layers increases (Figure 3.14 (a)).

To further validate the proposed explanation, two other printing modes were explored for the multi-layer lines, namely bidirectional printing and multiple-pass printing. Figure 3.14 (b) shows the morphologies of the printed lines using these two modes. Both lines appeared to be more uniform than the corresponding unidirection-

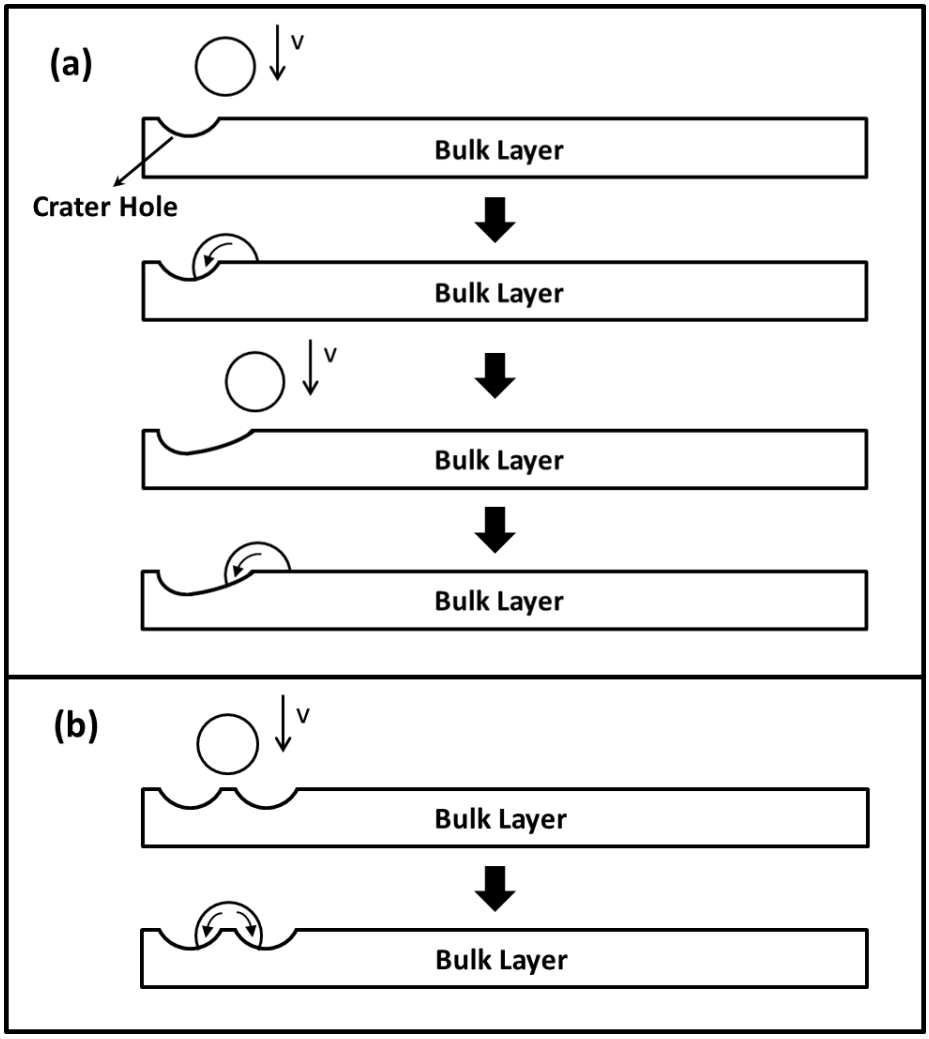

Figure 3.16. A crater hole is formed in the bulk layer after the drop evaporates. (a) When a line is printed unidirectionally with long time between adjacent drops, the deposited drops consistently slip into the hole due to gravity. (b) When a line is printed in 2 passes, the drops in the second pass are immobilized on the two holes created by the drops in the first pass.

ally printed line (the fourth line in Figure 3.14 (a)). The improved uniformity in those two lines can be easily understood using the proposed crater-hole-based explanation.

When a line is printed bidirectionally (i.e. the odd layers are printed from left to right whereas the even layers are printed from right to left), the ink migration from right to left that takes place during the deposition of the odd layers is counterbalanced by the ink migration from left to right when the even layers are deposited. In this way the overall line uniformity is improved.

Multiple-pass printing [35], also known as multilevel matrix [41] or multilayer array [6], is one of the printing methods to increase the homogeneity of printed patterns. To use the multiple-pass technique to print a multi-layer line, separate drops with constant spacing are deposited in a row during the first pass. The same print patterns are repeated in the next few passes at certain offsets with respect to the first pass in order to fill the gaps left in the first pass as shown in Figure 3.14 (c). In this manner every layer of the line is printed.

For the second line in Figure 3.14 (b), the time between any two consecutive passes (i.e. the time from the last deposition in the n^{th} pass to the first deposition in the $(n+1)^{th}$ pass) was larger than the evaporation time of a single drop. Therefore when the drops in the $(n+1)^{th}$ pass arrived at the bulk layer, separate crater holes had been already formed by the drops in the n^{th} pass. The arrived drops were normally situated on two crater holes thus the slip motion of the drops to a specific direction was minimized. Figure 3.16 (b) shows the case of a 2-pass printing where the drops in the second pass land right in the middle of the two crater holes created by the drops in the first pass. The landed drops are immobilized because of equal potential to fall into the crater holes at either side. Essentially multiple-pass printing improves the uniformity of multi-layer lines by reducing the ink migration due to the slip motion of the deposited drops.

3.5 Fabrication of Conductive Traces

Sintering is typically an essential step involved in the fabrication of electrically conductive patterns with inkjet printing [8, 9]. By means of heating the printed pattern at an elevated temperature, any residual solvent is burnt off completely. Moreover, the conductive solute particles in the printed pattern are gathered together through diffusion process. In this way the electrical conductivity is enhanced significantly.

For the ink used in this study, sintering process also serves to thermally decompose the solute. Previous study has shown that the palladium hexadecanethiolate will be thermally decomposed at 230 °C in the oven [35]. After the thermal decomposition (technically also known as thermolysis), nearly pure palladium is obtained [35].

3.5.1 Unidirectional Printing with Short or Medium Time between Adjacent Drops

Figure 3.17 shows the multi-layer lines printed unidirectionally with short or medium time between adjacent drops after the sintering process. Comparing the multi-layer lines after sintering to those before sintering (Figure 3.12 (a) and (b)), we can see that the light color portions in the printed lines vanish after the sintering process. This is because the materials in those light color portions are fairly sparse. Apparently, printing multi-layer lines unidirectionally with short or medium time between adjacent drops results in unfavorable open electrical connections.

3.5.2 Optimized Multiple-pass Printing

Printing layer-by-layer with long time between adjacent drops either unidirectionally or bidirectionally makes the lines electrically conductive as it will be shown in the next section. However, the manufacturing throughput is severely sacrificed due to the low printing efficiency (< 4 Hz). To overcome this dilemma in conductivity per-

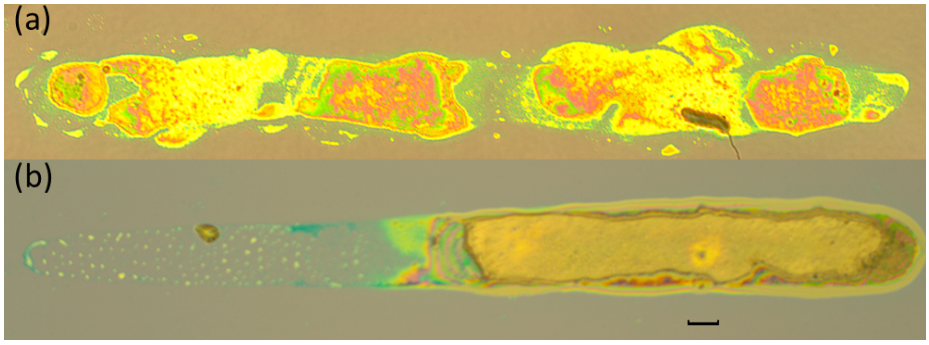

Figure 3.17. Sintered 15-layer lines that were printed unidirectionally with dot spacing 40 μm, time between adjacent drops (a) 10 ms (corresponding to the line in Figure 3.12 (a)); (b) 110 ms (corresponding to the line in Figure 3.12 (b)). The lines were sintered at 230 °C in the oven.

formance and manufacturing efficiency, an optimized multiple-pass printing routine was developed:

1. Determine the single drop diameter D_0 after complete evaporation.

2. Determine the highest reliable jetting frequency f_{max}. Experiments have shown that the highest reliable jetting frequency for the ink used in this study was about 800 Hz.

3. Determine the evaporation time for a single drop t_e.

4. Specify the dot spacing in a printed line d_s.

5. The drop pitch in each pass d_p is selected to be the minimum multiple of the dot spacing d_s without having any drops printed at this drop pitch overlapped. A necessary condition of d_p is $d_p = nd_s > D_0$ ($n \in \mathbb{N}^*$).

6. The number of passes n_p is determined by d_p/d_s.

7. Print at the highest jetting frequency f_{max} in each pass and ensure the time between any two consecutive passes is larger than the evaporation time of a single drop t_e.

A 15-layer line with dot spacing $d_s = 40$ μm was printed using the optimized multiple pass printing. The drop pitch in each pass $d_p = nd_s > D_0 = 125$ μm. Ideally the number of passes $n_p = n_{min} = 4$ and the drop pitch in each pass $d_p = n_p \cdot d_s = 160$ μm. However, in practice when the drops were printed at the drop pitch of 160 μm, there was still some chance to have two drops overlapped largely due to random variations of drop placement [42]. On the other hand, experiments showed that drops printed at the drop pitch of 200 μm were free from overlapping. Therefore the drop pitch d_p in each pass was finalized to be 200 μm with the number of passes $n_p = 5$. The drops in each pass were printed at the highest reliable jetting frequency (800 Hz). The time between two consecutive passes was ensured to be greater than the evaporation time of a single drop (250 ms) by printing one pass for another line between the two consecutive passes. Through analyzing the stage feedback velocity and position profile, the actual time between consecutive passes was found to be no less than 594 ms. After the first five passes, the first layer was deposited. The

remaining 14 layers were printed in the same way as the first layer. Figure 3.18 shows a 15-layer line printed with optimized 5-pass printing at the jetting frequency of 800 Hz.

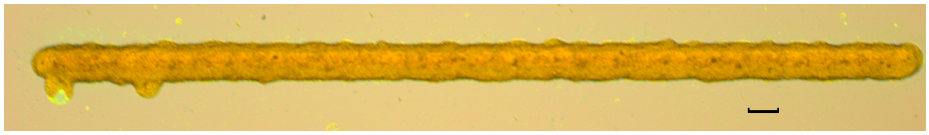

Figure 3.18. A 15-layer line with dot spacing 40 μm using optimized 5-pass printing at a jetting frequency of 800 Hz. The calibration bar represents 100 μm.

3.5.3 Comparison of Different Printing Methods

To evaluate the performances of lines printed with three different printing methods (i.e. unidirectional printing with a long time between adjacent drops , bidirectional printing with a long time between adjacent drops and optimized multiple-pass printing), 15-layer lines with dot spacing 40 μm were printed by three different methods: unidirectional printing with 290 ms between adjacent drops, bidirectional printing with 290 ms between adjacent drops and optimized 5-pass printing at the jetting frequency of 800 Hz. All the printed lines were sintered at the same condition on the hot plate at 250 °C for 1 h before further electrical characterization. Figure 3.19 shows the 15-layer line using optimized 5-pass printing after the sintering process.

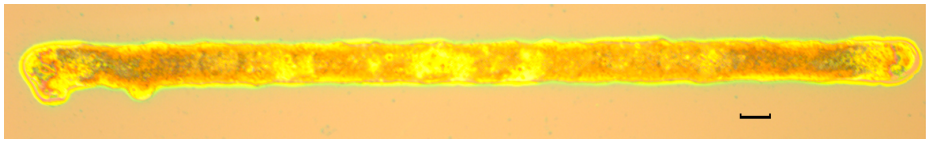

Figure 3.19. A sintered 15-layer line with dot spacing 40 μm using optimized 5-pass printing at the jetting frequency of 800 Hz. The line was obtained by sintering the printed line shown in Figure 3.18 at 250 °C on the hot plate for 1 hour.

The resistances of the lines were measured by placing 2 probes at the two ends of the lines. However, the measured resistances were not suitable to be directly used for evaluating the conductivity performances of different lines because the resistances were also influenced by where the two probes were placed. To eliminate the effect of the probe positions on the resistances, sheet resistances were adopted. For a general line resistance measurement using 2-probe method as shown in Figure 3.20, the sheet resistance $R_{\square}$ can be related to the measured resistance R by

$$R_{\square} = R(\int_0^L \frac{dx}{W(x)})^{-1}, \tag{3.25}$$

where L is the distance between the two probes and W is the width of the line.

Figure 3.20. Illustration of a general line resistance measurement using 2-probe method.

In order to compute the sheet resistances from the microscope images, a discrete form of Equation 3.25 based on the image pixels was used given by

$$R_{\square} = R(\sum_{i=1}^{N_p} \frac{1}{W_i})^{-1}, \tag{3.26}$$

where N_p is the number of pixels between the two probes, W_i is the width of the line in number of pixels at the i^{th} pixel.

In addition to the electrical conductivity, printing efficiency is also a very important index to evaluate a printing method. The required printing time for the same line patterns is a good indication of printing efficiency.

Figure 3.21 shows the I-V curve obtained by measuring the sintered line in Figure 3.19 using the 2-probe method. With the I-V curve being close to a straight line, the fabricated traces were considered to be well-behaved conductors.

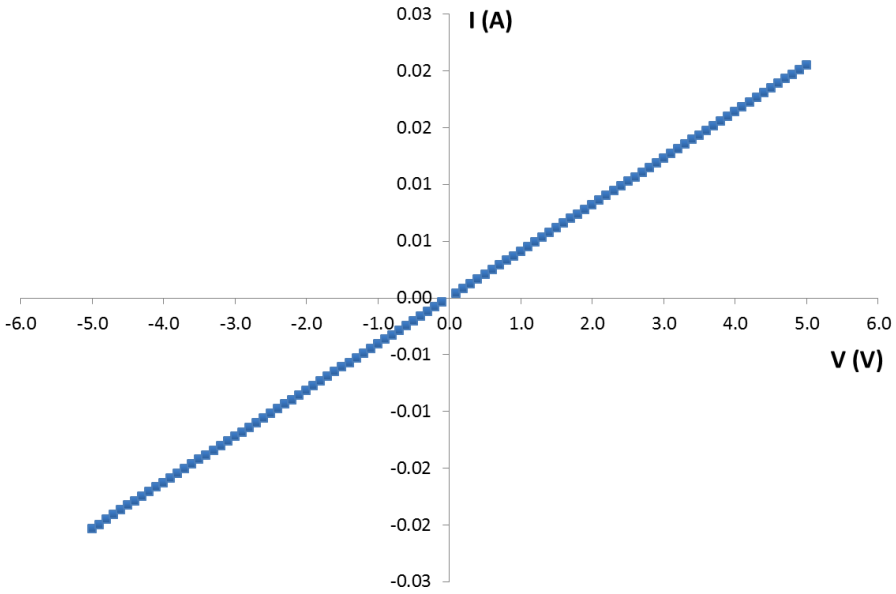

Figure 3.21. An I-V curve obtained by measuring the sintered line shown in Figure 3.19 using the 2-probe method. Square dots are measured data points. Based on the I-V curve, the resistance was found to be 244.7 Ω.

Table 3.1. Comparison of electrical resistances and printing efficiency.

Printing Methods	Sheet Resistance ($\Omega/\square$)	Print Time (s)
Unidirectional printing with 290 ms between adjacent drops	14.881 ± 0.741	326.3
Bidirectional printing with 290 ms between adjacent drops	14.268 ± 0.439	326.3
Optimized 5-pass printing @ 800 Hz	13.885 ± 0.411	1.3

Table 3.1 summarizes the sheet resistances and the required printing time for a 15-layer line with dot spacing 40 μm using different printing methods. The reported printing time is pure printing time, which excludes the stage acceleration and deceleration time.

As we can see, the optimized 5-pass printing yields the lowest sheet resistance thus the best electrical conductivity performance. This is because the amount of ink migration by multiple-pass printing is minimal among the three printing methods, which in turn results in the most uniform material distribution across a printed line. Moreover, in terms of printing efficiency, the optimized multiple-pass printing is two orders of magnitude better than the other two printing methods.

3.5.4 Optimized Multiple-pass Printing as a General Printing Routine

To successfully implement the optimized multiple-pass printing, one of the key steps is to allow enough time for the drop evaporation in one pass before the deposition of the adjacent drops in the next pass. Generally speaking, this is not a stringent condition to be met, especially for the volatile ink in which the evaporation time for each drop is relatively short. Instead of waiting for the drops in one pass to completely dry, one can print other patterns in the meantime. In this way the print

head is always operated at the maximum jetting frequency except during the time required to switch between different print patterns.

From the perspective of a general printing routine for fine line fabrication, there are several benefits to use the optimized multiple-pass printing:

- Printing is always operated at the highest reliable jetting frequency
- Dot spacing and jetting frequency can be designed independently as opposed to the conventional one-pass printing where the correct combination of dot spacing and jetting frequency is required in order to achieve the stable lines [16, 18, 19]. Dot spacing controls the number of drops per unit length, thus providing another degree of freedom to tune the line resistances.
- Minimum and uniform line width is ensured. Since the optimized multiple-pass printing ensures that every drop is deposited when the adjacent drops have completely evaporated, the width throughout a printed line is always about the diameter of a single drop, which is the smallest length scale that can be produced by inkjet printing.

4. CONCLUSIONS AND FUTURE WORK

This research work presents an experiment-based study of printed line morphologies using volatile ink in the presence of contact angle hysteresis and NRCA for the fabrication of electrical conductive traces.

If a single-layer line is printed with short time between adjacent drops so that the contact line of the bead is still pinned as it merges with the arriving droplet, one or several agglomerations are formed in the middle of the line. The exact fluid dynamics that leads to the formation of those agglomerations is still unclear at the moment and requires further investigation. If a line is printed with medium time between adjacent drops so that the bead has already depinned from the contact line prior to the arrival of the next droplet, only one agglomeration is formed and is always situated at the end of the line. This is because the amount of ink evaporation during the time between adjacent drops causes the molar concentration of the bead to be considerably higher than that of the newly deposited droplets, which results in the lower surface tension of the bead because of the positive surface excess of the solute. A hydrodynamic flow induced by this surface tension gradient consistently drives the bead to the fresh deposited droplet. In addition, a chain of overlapped drop ring deposits are formed within a line. The drop ring size initially increases with the number of depositions at a decreasing increment before it reaches or oscillates about an equilibrium. The equilibrium ring size decreases when the time between adjacent drops increases. If a line is printed with long time between adjacent drops so that the bead is dry at every deposition, no agglomeration is formed in this case and the width of the line is about the diameter of a single drop.

Multi-layer lines printed unidirectionally with short or medium time between adjacent drops have agglomerations, which are explained by the accumulations of agglomerations that take place in every layer. A multi-layer line printed unidirectionally

with long time between adjacent drops exhibits non-uniformity with the beginning of the line appearing darker than the end of the line. The trend becomes more profound as the number of layers increases. This is because the deposited drops dissolve the bulk layer, leaving a crater-like hole in the bulk and the drops consistently slip into the hole due to gravity. The uniformity of the line is improved by printing bidirectionally with long time between adjacent drops or using multiple-pass printing.

For conductive trace fabrication, printing multi-layer lines unidirectionally with short or medium time between adjacent drops results in open electrical connections after the sintering process. Printing layer-by-layer with long time between adjacent drops either unidirectionally or bidirectionally makes the lines electrically conductive. However, the manufacturing throughput is severely sacrificed due to the low printing efficiency. An optimized multiple-pass printing is developed so that the printing is always operated at the highest reliable jetting frequency. The optimized multiple-pass printing yields the best electrical conductivity among the three viable printing methods because the amount of ink migration by multiple-pass printing is minimal, which in turn results in the most uniform material distribution across a line. The line printed with the optimized multiple passes has the width of about a single drop diameter, which is the minimum length scale that can be produced by inkjet printing.

LIST OF REFERENCES

LIST OF REFERENCES

[1] S. Cho, J. Ko, J. Jung, J. Lee, D. Choi, and C. Lee. High-performance organic thin film transistors based on inkjet-printed polymer/TIPS pentacene blends. *Organic Electronics*, 13(8):1329–1339, August 2012.

[2] K. Kordás, T. Mustonen, G. Tóth, H. Jantunen, M. Lajunen, C. Soldano, S. Talapatra, S. Kar, R. Vajtai, and P. Ajayan. Inkjet printing of electrically conductive patterns of carbon nanotubes. *Small (Weinheim an der Bergstrasse, Germany)*, 2(8-9):1021–5, August 2006.

[3] H. Al-Chami and E. Cretu. Inkjet printing of microsensors. In *IEEE 15th International Mixed-Signals, Sensors, and Systems Test Workshop*, pages 1–6, 2009.

[4] S. Bathurst and S. Kim. Designing direct printing process for improved piezoelectric micro-devices. *CIRP Annals - Manufacturing Technology*, 58(1):193–196, January 2009.

[5] J. Kim, S. Na, and H. Kim. Inkjet printing of transparent InZnSnO conducting electrodes from nano-particle ink for printable organic photovoltaics. *Solar Energy Materials and Solar Cells*, 98:424–432, March 2012.

[6] A. Haldar, K. Liao, and S. Curran. Effect of printing parameters and annealing on organic photovoltaics performance. *Journal of Materials Research*, 27(16):2079–2087, July 2012.

[7] E. Roth, T. Xu, M. Das, C. Gregory, J. Hickman, and T. Boland. Inkjet printing for high-throughput cell patterning. *Biomaterials*, 25(17):3707–15, August 2004.

[8] C. Kim, M. Nogi, K. Suganuma, and Y. Yamato. Inkjet-Printed Lines with Well-Defined Morphologies and Low Electrical Resistance on Repellent Pore-Structured Polyimide Films. *ACS applied materials interfaces*, 2012.

[9] C. Kim, M. Nogi, and K. Suganuma. Electrical conductivity enhancement in inkjet-printed narrow lines through gradual heating. *Journal of Micromechanics and Microengineering*, 22(3):3–8, March 2012.

[10] H. Lee, K. Chou, and K. Huang. Inkjet printing of nanosized silver colloids. *Nanotechnology*, 16(10):2436–2441, October 2005.

[11] E. Chibowski and F. Gonzalez-Caballero. Interpretation of contact angle hysteresis. *Journal of adhesion science and technology*, 7(11):1195–1209(15), 1993.

[12] R. Johnson and R. Dettre. Contact angle hysteresis. III. Study of an idealized heterogeneous surface. *The Journal of Physical Chemistry*, 107(43):1744–1750, 1964.

[13] P. de Gennes. Wetting: statics and dynamics. *Reviews of Modern Physics*, 57(3):827–863, 1985.

[14] C. Lam, R. Wu, D. Li, M. Hair, and A. Neumann. Study of the advancing and receding contact angles: liquid sorption as a cause of contact angle hysteresis. *Advances in colloid and interface science*, 96(1-3):169–91, February 2002.

[15] S. Davis. Moving contact lines and rivulet instabilities. Part 1. The static rivulet. *Journal of Fluid Mechanics*, 98(02):225–242, April 1980.

[16] P. Duineveld. The stability of ink-jet printed lines of liquid with zero receding contact angle on a homogeneous substrate. *Journal of Fluid Mechanics*, 477(-1):175–200, March 2003.

[17] J. Stringer and B. Derby. Limits to feature size and resolution in ink jet printing. *Journal of the European Ceramic Society*, 29(5):913–918, March 2009.

[18] J. Stringer and B. Derby. Formation and stability of lines produced by inkjet printing. *Langmuir The ACS Journal Of Surfaces And Colloids*, 26(12):10365–10372, June 2010.

[19] D. Soltman and V. Subramanian. Inkjet-printed line morphologies and temperature control of the coffee ring effect. *Langmuir The ACS Journal Of Surfaces And Colloids*, 24(5):2224–2231, 2008.

[20] P. Thomas and A. Lavanya. Self-assembling bilayers of palladiumthiolates in organic media. *Journal of Chemical Sciences*, 113(December):611–619, 2001.

[21] W. Boley, C. Shou, and G. Chiu. Drop coalescence for an inkjet printed functional film: how avoiding coalescence can improve functional performance (working paper).

[22] R. Rioboo, M. Marengo, and C. Tropea. Time evolution of liquid drop impact onto solid , dry surfaces. *Experiments in Fluids*, 33(1):112–124, 2002.

[23] W. Hsiao, S. Hoath, G. Martin, and I. Hutchings. Ink Jet Printing for Direct Mask Deposition in Printed Circuit Board Fabrication. *Journal of Imaging Science and Technology*, 53(5):050304, 2009.

[24] M. Pasandideh-Fard, Y. Qiao, S. Chandra, and J. Mostaghimi. Capillary effects during droplet impact on a solid surface. *Physics of Fluids*, 8(3):650, 1996.

[25] L. Tanner. The spreading of silicone oil drops on horizontal surfaces. *Journal of Physics D: Applied Physics*, 12(1838):1473–1484, 1979.

[26] R. Deegan, O. Bakajin, T. Dupont, G. Huber, S. Nagel, and T. Witten. Capillary flow as the cause of ring stains from dried liquid drops. *Nature*, 389(6653):827–829, 1997.

[27] R. Deegan. Pattern formation in drying drops. *Physical Review E Statistical Physics Plasmas Fluids And Related Interdisciplinary Topics*, 61(1):475–85, 2000.

[28] C. Tropea, A. Yarin, and J. Foss. *Springer Handbook of Experimental Fluid Mechanics, Volume 1*. Springer-Verlag New York, LLC, 2007.

[29] A. Adamson. *Physical Chemistry of Surfaces 2nd Edition*. Interscience Publishers, New York, N.Y., 1967.

[30] N. Lange. *Lange's Handbook of Chemistry 10th Edition*. 1967.

[31] S. Schiaffino and A. Sonin. Formation and stability of liquid and molten beads on a solid surface. *Journal of Fluid Mechanics*, 343(-1):95–110, July 1997.

[32] S. David, K. Sefiane, and L. Tadrist. Experimental investigation of the effect of thermal properties of the substrate in the wetting and evaporation of sessile drops. *Colloids and Surfaces A Physicochemical and Engineering Aspects*, 298(1-2):108–114, April 2007.

[33] D. Redinger, S. Molesa, S. Yin, R. Farschi, and V. Subramanian. An ink-jet-deposited passive component process for RFID. *IEEE Transactions on Electron Devices*, 51(12):1978–1983, 2004.

[34] J. Kang, H. Kim, J. Ryu, H. Thomas Hahn, S. Jang, and J. Joung. Inkjet printed electronics using copper nanoparticle ink. *Journal of Materials Science Materials in Electronics*, 21(11):1213–1220, January 2010.

[35] W. Boley, T. Bhuvana, B. Hines, and R. Sayer. Inkjet Printing Involving Palladium Alkanethiolates and Carbon Nanotubes Functionalized with Single-Strand DNA. In *NIP 25: DIGITAL FABRICATION 2009, TECHNICAL PROGRAM AND PROCEEDINGS*, pages 824–827, 2009.

[36] Y. Gizachew, L. Escoubas, J. Simon, M. Pasquinelli, J. Loiret, P. Leguen, J. Jimeno, J. Martin, A. Apraiz, and J. Aguerre. Towards ink-jet printed fine line front side metallization of crystalline silicon solar cells. *Solar Energy Materials and Solar Cells*, 95(1):S70–S82, May 2011.

[37] T. Wang, M. Roberts, I. Kinloch, and B. Derby. Inkjet printed carbon nanotube networks: the influence of drop spacing and drying on electrical properties. *Journal of Physics D: Applied Physics*, 45(31):315304, August 2012.

[38] T. Kawase, H. Sirringhaus, R. Friend, and T. Shimoda. Inkjet Printed Via-Hole Interconnections and Resistors for All-Polymer Transistor Circuits. *Advanced Materials*, 13(21):1601–1605, November 2001.

[39] Y. Xia and R. Friend. Nonlithographic patterning through inkjet printing via holes. *Applied Physics Letters*, 90(25):253513, 2007.

[40] A. Lennon, A. Ho-Baillie, and S. Wenham. Maskless patterned etching of silicon dioxide by inkjet printing. *2008 Conference on Optoelectronic and Microelectronic Materials and Devices*, 2052:170–173, 2008.

[41] E. Tekin, B. Gans, and U. Schubert. Ink-jet printing of polymersfrom single dots to thin film libraries. *Journal of Materials Chemistry*, 14(17):2627–2632, 2004.

[42] W. Boley, R. Sayer, and G. Chiu. Stochastic Modelling of Drop Coalescence on Non-Porous Substrates for Inkjet Applications. In *2011 ASME Dynamic Systems and Control Conference, Arlington,2011 ASME Dynamic Systems and Control Conference, Arlington, VA, OCT 31 - NOV 2.*, 2011.

[43] I. Hutchings, G. Martin, and S. Hoath. High speed imaging and analysis of jet and drop formation. *Journal of Imaging Science*, 51(5):438–444, 2007.

[44] H. Dong, W. Carr, and J. Morris. An experimental study of drop-on-demand drop formation. *Physics of Fluids*, 18(7):072102, 2006.

APPENDICES

A. DROPLET EJECTION SPEED MEASUREMENT

Flash photography is a widely used visualization technique to measure droplet ejection speed from a nozzle of an inkjet print head by taking pictures of successive droplet events at known temporal instants [43,44]. Here I propose a novel method to measure the droplet ejection speed with reasonable accuracy without utilizing any cameras.

An image consisting of equidistant dots in a vertical line was printed bidirectionally at a high stage velocity v_s with a known standoff distance Z between the print head and the substrate. Since it took some time for a droplets to reach the surface of the substrate after the droplets left the nozzle, the actual drop positions had some offsets with respect to the triggering positions. The direction of the offset was dependent on the print head scan direction. Since the image was printed bidirectionally, the final printed image appeared to be somewhat zigzagged as shown in Figure A.1. The offset between two columns of dots d could be obtained through image analysis. Then the time for a droplet to reach the substrate after ejection T was found by

$$T = \frac{d}{2v_s}. \tag{A.1}$$

And the ejection speed v_e was found by

$$v_e = \frac{Z}{T}. \tag{A.2}$$

The time for a droplet to reach the substrate T varied linearly with the standoff distance Z as shown in Figure A.2. The ejection speed was the slope of the best linear fit to the data (5.031 m/s).

Due to the limitation of lab equipment, this method has not been cross verified with the conventional optical method. However, with linear regression coefficient being close to 1 and the measured speed being within the typical range in the literature (1 - 10 m/s), the measured ejection speed is considered to be valid.

Figure A.1. Equidistant dots in a vertical line were printed bidirectionally with a drop pitch 250 μm and a stage scanning speed 225 mm/s. The scan direction was defined as the relative motion of the print head with respect to the substrate.

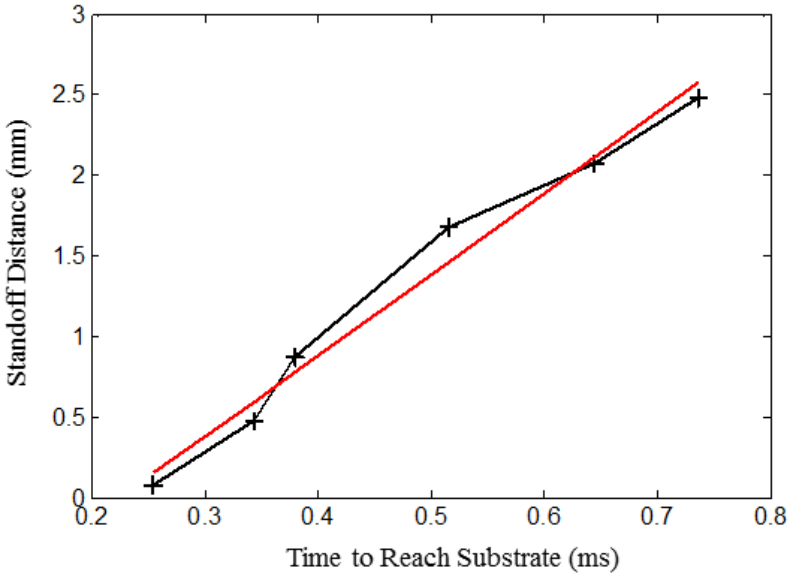

Figure A.2. The time for a droplet to reach the substrate varied linearly with the standoff distance. Linear regression (red line) fit the experimental data (plus signs) with coefficient R2 of 0.98. The ejection speed was the slope of the linear fit (5.031 m/s).

B. TIME DURATION OF DROP WETTING PHASE

The drop diameter during the wetting phase follows the Tanner's law [25]

$$\frac{D(t)}{D_i} = k(\frac{v_e t}{D_i})^{0.1}, \tag{B.1}$$

where $D(t)$ is the drop diameter, D_i is the droplet diameter prior to impact, v_e is the droplet ejection speed, k is a constant.

The maximum spreading drop diameter D_m can be found by

$$D_m = \beta_m D_i, \tag{B.2}$$

where β_m is the maximum spreading factor.

The maximum spreading factor β_m was found within the range of 2.37 - 2.45. The droplet diameter prior to impact D_i was found to be about 44 μm. Based on the Equation B.2, the maximum spreading drop diameter D_m was found to be 104.28 - 107.8 μm, which was smaller than the equilibrium drop diameter D_e ($\sim$ 125 μm). This indicated that the drop did not go through oscillation and retraction during the relaxation phase. Furthermore, the drop continued to spread on the substrate in the wetting phase due to the capillary effect.

The initial drop diameter in the wetting phase was no less than the maximum spreading diameter D_m. The time for the impact phase t_i and the time for the relaxation phase t_r were respectively 23 μs and 70 - 100 μs. Therefore the beginning time of the wetting phase $t_{w1} = t_i + t_r$ = 93 - 123 μs. Based on Equation B.1, the end time of the wetting phase t_{w2} could be found by

$$t_{w2} = (\frac{D_e}{D_m})^{10} t_{w1}. \tag{B.3}$$

Using Equation B.3, the upper bound of t_{w2} was found to be 0.753 ms when D_m = 104.28 μm and t_{w1} = 123 μs. Therefore the time of drop wetting phase t_w was equal to $(t_{w2} - t_{w1})$ no larger than 0.63 ms.